

Gravitational waves from the electroweak phase transition

Leonardo Leitao*, Ariel Mégevand† and Alejandro D. Sánchez‡

IFIMAR (CONICET-UNMdP)

*Departamento de Física, Facultad de Ciencias Exactas y Naturales,
UNMdP, Deán Funes 3350, (7600) Mar del Plata, Argentina*

Abstract

We study the generation of gravitational waves in the electroweak phase transition. We consider a few extensions of the Standard Model, namely, the addition of scalar singlets, the minimal supersymmetric extension, and the addition of TeV fermions. For each model we consider the complete dynamics of the phase transition. In particular, we estimate the friction force acting on bubble walls, and we take into account the fact that they can propagate either as detonations or as deflagrations preceded by shock fronts, or they can run away. We compute the peak frequency and peak intensity of the gravitational radiation generated by bubble collisions and turbulence. We discuss the detectability by proposed spaceborne detectors. For the models we considered, runaway walls require significant fine tuning of the parameters, and the gravitational wave signal from bubble collisions is generally much weaker than that from turbulence. Although the predicted signal is in most cases rather low for the sensitivity of LISA, models with strongly coupled extra scalars reach this sensitivity for frequencies $f \sim 10^{-4}$ Hz, and give intensities as high as $h^2\Omega_{\text{GW}} \sim 10^{-8}$.

1 Introduction

Several gravitational wave (GW) detectors are currently planned to be constructed in space [1, 2, 3, 4, 5, 6]. The laser interferometer space antenna (LISA) [2, 3] is designed to detect the passage of a gravitational wave by measuring the time-varying changes of optical pathlength between free-falling masses. LISA consists of three spacecraft in heliocentric orbits, forming a triangle with sides $\sim 10^9$ m long. The LISA program was born more than ten years ago as a joint project of ESA and NASA. Recently, a variant of LISA was proposed, which is called New Gravitational wave Observatory (NGO) or evolved

*E-mail address: lleitao@mdp.edu.ar

†Member of CONICET, Argentina. E-mail address: megevand@mdp.edu.ar

‡Member of CONICET, Argentina. E-mail address: sanchez@mdp.edu.ar

LISA (eLISA). The Big Bang observer (BBO) [4] has been proposed as the successor of LISA. BBO is composed of four LISA type space detectors orbiting the sun, two of them collocated. In this case the arm length is $\sim 10^7$ m. A Japanese project with similar characteristics is the Deci-Hertz Interferometer Gravitational-wave Observatory (DECIGO) [5, 6]. The latter detectors would bridge the frequency gap between LISA and terrestrial detectors.

These GW observatories will be able to measure a stochastic background of cosmological origin [7, 8, 9]. The detection of a primordial background of gravitational radiation would provide a direct probe of the physics in the early Universe, since GWs propagate freely after being produced. Cosmological sources of gravitational radiation include quantum fluctuations during inflation (see, e.g., [10]), scalar condensate fragmentation into Q-balls [11], cosmic strings (see, e.g., [12]), plasma turbulence and magnetic fields (see, e.g., [13, 14]). A possible scenario for the generation of a primordial GW background is a first-order phase transition of the Universe [15, 16, 17]. Quite interestingly, GWs produced at the temperature scale of the electroweak phase transition, $T_* \sim 100$ GeV, would have a characteristic frequency today (after redshifting) near the sensitivity peak of LISA, $f \sim 1$ mHz. This motivated the investigation of GW production in the electroweak phase transition [18, 19, 20, 21, 22, 23].

In a first-order phase transition, bubbles of the stable phase nucleate and expand, converting the high-temperature phase into the low-temperature one (for the dynamics of a cosmological first-order phase transition see, e.g., [24, 25, 26] and references therein). Gravitational waves are generated either by the collisions of bubbles [15, 16, 17, 27, 28] or by the turbulence that is produced in the plasma due to the motion of bubble walls [17, 29, 30, 31, 32]. In general, turbulence turns out to be a more effective source of gravitational radiation than bubble collisions. In the Standard Model (SM), the electroweak phase transition is not first-order [33]. As a consequence, the disturbance caused in the fluid is not enough to generate a significant GW signal. Models which give strongly first-order phase transitions and, consequently, a greater departure from equilibrium have been extensively studied in the context of electroweak baryogenesis [34].

The GW production can be calculated as a function of a few quantities related to the dynamics of the phase transition (see, e.g., [13, 14, 15, 16, 17, 27, 32]). These quantities are the temperature, the bubble wall velocity, the bubble size (or the duration of the phase transition), and the fraction of the released energy which goes into bulk motions of the fluid (the efficiency factor). The latter can be calculated as a function of the amount of supercooling and the wall velocity [17]. Furthermore, the wall is usually assumed to propagate as a Jouguet detonation, so that the wall velocity and the efficiency factor have a simple dependence on the amount of supercooling. This motivated some model-independent analysis which find the electroweak GW spectrum as a function of two parameters, namely, the duration of the phase transition and the amount of supercooling (see, e.g., [19]). In a given model, though, these parameters are linked, and it is important to investigate specific cases. Such investigations were performed, e.g., in Refs. [18, 20, 22, 23].

However, it is well known that the wall velocity does not only depend on the amount of supercooling but also on the friction with the surrounding plasma. In general, the hydrodynamic solution is not a Jouguet detonation. Contrary to the case of gravitational

waves, calculations of electroweak baryogenesis usually assume small wall velocities. The bubble growth mechanism has been studied for several years (see, e.g., [35]). Recently, there has been a renewed interest. The wall velocity was calculated taking into account hydrodynamics and microphysics in Refs. [36, 37, 38]. In Ref. [39] the microphysics in the ultra-relativistic regime was considered, finding that bubble walls may run away. The efficiency factor was calculated as a function of the wall velocity in Ref. [21] for deflagrations and, more recently, in Refs. [38, 40] for the whole range of wall velocities.

In the present paper we study the generation of gravitational waves in the electroweak phase transition. We consider physical models and we include in the calculation some aspects of the dynamics which have not been taken into account previously. In particular, we incorporate the recent results on the hydrodynamics and microphysics of moving walls. We follow the evolution of the phase transition, taking into account the nucleation and expansion of bubbles, and the variation of temperature. We also take into account the effect of temperature inhomogeneities on the nucleation rate. We consider extensions of the SM with extra bosons, extra fermions, and the MSSM in the light-stop scenario. Our aim is to discuss the detectability of the gravitational radiation by LISA and other proposed detectors. Thus, we calculate the peak of the GW spectrum from bubble collisions and from turbulence, as a function of the parameters of each model. In this work we shall ignore the possible presence of magnetic fields, which would modify the turbulence mechanism [32, 41].

The plan of the paper is the following. In the next section we review the mechanisms for generation of gravitational waves by turbulence and bubble collisions. In section 3 we consider the nucleation, expansion and collisions of bubbles, and the energy injected into bulk motions of the fluid. We shall use results from Refs. [36, 37, 42] for the wall velocity, and results from Ref. [40] for the kinetic energy of the fluid. In section 4 we write down the one-loop finite-temperature effective potential which we shall use to calculate the thermodynamic parameters and the evolution of the phase transition. We also consider the general expression for the friction and the condition for “runaway” walls. In section 5, we solve the equations for the dynamics of the phase transition and calculate the peak frequency and energy density of GWs. In section 6 we compare the signals obtained for the different models, and we discuss the possibility of observation at several planned space-based GW antennas. Finally, in section 7 we summarize our conclusions.

2 Gravitational wave generation

The energy density of gravitational radiation is usually expressed in terms of the quantity

$$h^2\Omega_{\text{GW}}(f) = \frac{h^2}{\rho_c} \frac{d\rho_{\text{GW}}}{d\log f}, \quad (1)$$

where ρ_{GW} is the energy density of the GWs, f is the frequency, and ρ_c is the critical energy density today, defined by $\rho_c = 3H_0^2/(8\pi G)$, where $H_0 = 100 h \text{ km s}^{-1} \text{ Mpc}^{-1}$ is the present day Hubble expansion rate, with $h \simeq 0.72$ [43], and G is Newton’s constant. Alternatively, the GW spectrum is often given in terms of the characteristic amplitude h_c

or the root spectral density \sqrt{S} . These are related to $h^2\Omega_{\text{GW}}$ by [1]

$$h^2\Omega_{\text{GW}} = \left(\frac{f}{\text{Hz } 1.263 \times 10^{-18}} \frac{h_c}{1} \right)^2, \quad (2)$$

$$h_c = \sqrt{2fS}. \quad (3)$$

We shall consider the generation of GWs by bulk motions of the plasma during the electroweak phase transition.

2.1 General features of GWs from bulk motions of the plasma

For GWs originated at a time t_* , a frequency f_* redshifted to today is given by $f_0 = f_* a_*/a_0$, where the ratio of the scale factor at $t = t_*$ to the scale factor today is given by the adiabatic expansion relation $(g_0 T_0^3)/(g_* T_*^3) = a_*^3/a_0^3$, where g_0, T_0 and g_*, T_* are the number of relativistic degrees of freedom (d.o.f.) and the temperature today and at $t = t_*$, respectively. We have

$$\frac{a_*}{a_0} \approx 8 \times 10^{-16} \left(\frac{100}{g_*} \right)^{1/3} \frac{100 \text{ GeV}}{T_*}. \quad (4)$$

The typical wavelength will be a fraction of the Hubble size H_*^{-1} . Therefore, it is convenient to consider f_*/H_* , where the Hubble rate is given by the Friedmann equation,

$$H_*^2 = \frac{8\pi G}{3} \rho_*. \quad (5)$$

Here, $\rho_* = \rho_{R*} + \rho_{\text{vac}}$ is the total energy density, where $\rho_{R*} = \pi^2 g_* T_*^4/30$ is the energy density of radiation and ρ_{vac} is the false vacuum energy density. Thus, we can express the frequency of the GWs today as

$$f_0 = 1.6 \times 10^{-5} \text{ Hz} \left(\frac{g_*}{100} \right)^{1/6} \left(\frac{T_*}{100 \text{ GeV}} \right) \frac{f_*}{H_*}. \quad (6)$$

The characteristic frequency is determined by the typical length scale of the source L_S . Thus, one expects the peak of the spectrum to be at a frequency $f_* \sim 1/L_S$.

The energy density of gravitational waves is given by [7] $\rho_{\text{GW}}(\mathbf{x}, t) \sim \langle \partial_t h_{\mu\nu} \partial_t h^{\mu\nu} \rangle / G$, where $h_{\mu\nu}$ is the tensor metric perturbation, and the brackets denote ensemble average. The equation for $h_{\mu\nu}$ is of the form $\square h_{\mu\nu} \sim G T_{\mu\nu}$, where $T_{\mu\nu}$ is the energy-momentum tensor of the source. On dimensional grounds, one expects the magnitude of $h_{\mu\nu}$ to be given by $L_S^{-2} h \sim G \rho_K$, where ρ_K is the average kinetic energy density in bulk motions of the relativistic fluid. Similarly, we expect $\partial_t h \sim G \rho_K L_S$. Therefore, we have $\rho_{\text{GW}} \sim G \rho_K^2 L_S^2$. Using Eq. (5), this gives $\rho_{\text{GW}*} \sim (\rho_K/\rho_*)^2 (L_S H_*)^2 \rho_*$. After the phase transition, the total energy density ρ_* goes into radiation, and then evolves as $(a_*/a_0)^4$. Since ρ_{GW} dilutes like radiation, we have today $\rho_{\text{GW}0} \sim (\rho_K/\rho_*)^2 (L_S H_*)^2 \rho_{R0}$. The energy density of radiation today is given by $\rho_{R0}/\rho_c \equiv \Omega_R \approx 5 \times 10^{-5}$ [43]. This estimate gives, for the

amplitude of the GW spectrum today¹,

$$\Omega_{\text{GW}} \sim \left(\frac{\rho_K}{\rho} \right)_*^2 (L_S H)_*^2 \Omega_R. \quad (7)$$

In a first-order phase transition, the moving walls of expanding bubbles cause perturbations in the cosmic fluid. The bulk motions of the fluid produce GWs once bubbles collide and lose their spherical symmetry. In addition, bubble collisions generate turbulence, which is another source of GWs.

2.2 Gravitational waves from turbulence and bubble collisions

Let us first consider bubble collisions. A simulation with a large number of bubbles was carried out in Ref. [27] using the envelope approximation. This approximation neglects the overlap regions of colliding bubbles and follows only the evolution of the uncollided bubble walls (assuming thin fluid profiles). In Ref. [27] the bubbles were assumed to nucleate with a rate per volume and time given by

$$\Gamma(t) = \Gamma(T_i) \exp[\beta(t - t_i)], \quad (8)$$

and to expand with a constant velocity v_w . The result for the peak frequency and intensity from the simulation is [27]

$$f_p^{\text{coll}} = 1.6 \times 10^{-5} \text{ Hz} \left(\frac{0.62}{1.8 - 0.1v_w + v_w^2} \right) \left(\frac{g_*}{100} \right)^{1/6} \frac{T_*}{100 \text{ GeV}} \frac{\beta}{H_*}, \quad (9)$$

$$\Omega_p^{\text{coll}} = 0.33 \left(\frac{100}{g_*} \right)^{1/3} \frac{0.11v_w^3}{0.42 + v_w^2} \left(\frac{\rho_K}{\rho} \right)_*^2 \left(\frac{H}{\beta} \right)_*^2 \Omega_R. \quad (10)$$

This result agrees with Eqs. (6) and (7), except for a slight difference in the dependence on v_w . This can be seen by assuming $L_S \sim 2v_w\beta^{-1}$, since the time scale in this simulation is given by β . The parameter β does not depend on details of the dynamics of the phase transition and is relatively easy to estimate for a given model. According to Eq. (8), we have

$$\beta = \dot{\Gamma}/\Gamma. \quad (11)$$

The temperature decrease rate is governed by the Hubble rate, $dT/dt \simeq -HT$. Hence, we have

$$\frac{\beta}{H} = -\frac{T}{\Gamma} \frac{d\Gamma}{dT}. \quad (12)$$

Concerning turbulence, one expects that eddies of a given scale L_S will generate GWs with frequency given by $f_* \sim 1/L_S$ and energy density given by Eq. (7). The size distribution of the eddies, as well as the energy distribution of the turbulence, is difficult to determine. In general, a single stirring scale L_S is assumed in the calculation. Below this scale, a Kolmogorov spectrum is established, according to which eddies of a given

¹The ratio ρ_K/ρ is related to the generally used parameters κ (the efficiency factor) and α (defined in section 3.1) by $(\rho_K/\rho)_* = \kappa\alpha/(1 + \alpha)$ [notice that $(\rho_K/\rho_R)_* = \kappa\alpha$].

size break into smaller ones. This generates a cascade of energy which ends at a much smaller scale, related to the viscosity of the fluid. Above the stirring scale, the spectrum is determined by causality. In Ref. [13], these two behaviors were assumed on each side of the stirring scale. In this case, the result for the peak agrees with the estimate (7). More recently [32], turbulence was modeled using a smooth interpolation between the large scale behavior and the small scale one. Besides, the fact that turbulence lasts for several Hubble times was taken into account. According to these results, the peak frequency is shifted to $f_{p*} \simeq 3.5/L_S$. Using the bubble size, $L_S \approx 2R_b$, Eq. (6) gives

$$f_p^{\text{turb}} = 2.7 \times 10^{-5} \text{ Hz} \left(\frac{g_*}{100} \right)^{1/6} \left(\frac{T_*}{100 \text{ GeV}} \right) \frac{1}{H_* R_b}. \quad (13)$$

A fit to the result of Ref. [32] for the GW spectrum is given in Ref. [44] (see also [9]). The parametric dependence changes with respect to the estimate (7). For the peak intensity we have

$$\Omega_p^{\text{turb}} = 0.63 \left(\frac{\rho_K}{\rho} \right)_*^{3/2} \left(\frac{(R_b H)_*}{1 + 4 \frac{3.5\pi}{(R_b H)_*}} \right) \Omega_R. \quad (14)$$

Notice that, since $(R_b H)_* \lesssim 1$, the dependence on the spatial scale in Eq. (14) is practically that of Eq. (7), $\Omega_p^{\text{turb}} \propto (R_b H)_*^2$.

2.3 Characteristic size scales

As pointed out in Ref. [20], deciding which bubble size is relevant for turbulence is a major source of uncertainty. Bubbles of different sizes are present at the collision time. The bubbles of a given size stir up the fluid at that size scale, hence producing eddies of that scale. Larger bubbles in principle generate larger eddies and a larger GW intensity, whereas smaller bubbles in principle generate smaller eddies, but are more abundant. In any case, it is not clear which will be the turbulence spectrum in the case of several stirring scales. Although last nucleated bubbles are more abundant, they act during a shorter time and, furthermore, are probably “eaten” by larger bubbles. In our numerical calculations we shall use the size of the largest bubbles at percolation. Notice that, in contrast, there is no ambiguity in the production of GWs through bubble collisions, since the numerical fit (9)-(10) was obtained as a function of the parameters used in the simulation [27]. There is only some arbitrariness in the temperature at which the parameter β should be calculated, since in a real phase transition β is not a constant.

We can obtain a simple estimate of the bubble size dispersion if we assume a nucleation rate of the form (8) and a constant wall velocity, and we neglect bubble overlapping. The bubbles which nucleated at time t have a radius $R_b(t, t_p) = v_w(t_p - t)$ at the percolation time t_p , and occupy a volume $dV \propto \Gamma(t) R_b(t, t_p)^3$. Thus, for the largest bubbles, which nucleated at time t_i , we have

$$R_{\text{max}} \approx v_w(t_p - t_i). \quad (15)$$

On the other hand, the bubbles which occupy the largest volume are given by the condition $d(\Gamma R_b^3)/dt = 0$. Using Eq. (11), we see that the size R_V corresponding to the maximum of the volume distribution is given by

$$R_V = 3v_w/\beta(t_V). \quad (16)$$

This equation can be solved, taking into account that the nucleation time t_V is related to R_V through $R_V = v_w(t_p - t_V)$. The time t_V thus estimated should be between the nucleation time of the first bubbles t_i and the percolation time t_p . On the other hand, the duration of the phase transition is usually assumed to be $\Delta t \sim \beta^{-1}$, which gives for the largest bubbles

$$R_{\max} \sim v_w \beta^{-1}. \quad (17)$$

This approximation thus gives $R_{\max} \sim R_V$. However, one expects $R_V \ll R_{\max}$ due to the rapid variation of the nucleation rate. One could use the value $\beta^{-1}(t_p)$, which is larger than $\beta^{-1}(t_V)$, in Eq. (17). However, this will not solve the problem. As we shall see in the next section, the parameter β does not have a huge variation between t_i and t_p [this validates the approximation (8)], except for very strong phase transitions. In general, the variation of β will not even compensate the factor 3 between Eqs. (16) and (17). For very strong phase transitions, on the other hand, $\beta(t_p)$ may become negative. This indicates that the widely used approximation $\Delta t \approx \beta^{-1}$ for the duration of the phase transition should be refined for this application.

The estimate $\Delta t \sim \text{few}/\beta$ was obtained in Ref. [16], where in fact $\text{few} = \log(M/m)$, with $M \gg 1$ and $m \ll 1$. Notice that such a numerical factor in the bubble radius may be important. Indeed, the peak frequency (13) is proportional to $1/R_b$, whereas the intensity (14) is approximately² proportional to R_b^2 . We can estimate the factor as follows. The initial nucleation time is that at which there is a bubble in a Hubble volume. Roughly,

$$H^{-3} \int_{-\infty}^{t_i} \Gamma(t) dt \sim 1. \quad (18)$$

For a nucleation rate of the form (8) we obtain³ $\Gamma(T_i) \sim H^3 \beta$. The percolation time is roughly given by the condition

$$\int_{-\infty}^{t_p} \frac{4\pi}{3} v_w^3 (t_p - t)^3 \Gamma(t) dt \sim 1, \quad (19)$$

which yields $8\pi v_w^3 \Gamma(T_i) \exp[\beta(t_p - t_i)] \sim \beta^4$. Since $\Gamma(T_i) \sim H^3 \beta$, we have

$$t_p - t_i \sim 3 \log\left(\frac{\beta}{H}\right) \times \beta^{-1}. \quad (20)$$

As we shall see, Eq. (20) is indeed a good approximation. Hence, we see that $R_{\max}/R_V \sim \log(\beta/H)$. If the log is of order 1, then we have $t_p - t_i \sim \beta^{-1}$. However, this is not in general the case. In general we have $\beta \gg H$, since the bounce action varies very quickly. The value of β/H is usually assumed⁴ to be $\beta/H \sim 100$, which gives $t_p - t_i \gtrsim 10/\beta$. Indeed, as we shall see in the next section, in general we have $R_{\max}/R_V \gtrsim 10$. If the largest bubbles are relevant for turbulence instead of those of maximum volume, then the approximation $R_b \sim v_w \beta^{-1}$ in Eq. (14) leads to an underestimation of the GW signal from turbulence by at least two orders of magnitude.

²For $R_b H \lesssim 1$, the deviation from the law $\Omega_p^{\text{turb}} \propto R_b^2$ is at most a 2%.

³We see that the usual rough estimate $\Gamma(T_i) \sim H^4$ is valid only if $\beta \sim H$.

⁴As we shall see, β can depart significantly from this value.

3 Phase transition dynamics

As bubbles expand, latent heat is released at the phase boundary. Part of this energy raises the temperature of the plasma, and another part is converted into kinetic energy in bulk motions of the fluid. The system we consider consists of the fluid and the Higgs field ϕ . All the thermodynamic quantities (energy density, pressure, etc.) are derived from the free energy $\mathcal{F}(\phi, T)$. In a range of temperatures around the electroweak scale $T \sim 100$ GeV, the high-temperature minimum of \mathcal{F} , $\phi = 0$, coexists with a symmetry-breaking minimum $\phi_m(T)$. The minima are separated by a barrier. In the unbroken-symmetry phase, the free energy density is given by $\mathcal{F}_+(T) = \mathcal{F}(0, T)$, whereas in the broken-symmetry phase, it is given by $\mathcal{F}_-(T) = \mathcal{F}(\phi_m(T), T)$. For a given temperature T , the pressure in each phase is given by $p_{\pm}(T) = -\mathcal{F}_{\pm}(T)$, and the energy density is given by $\rho_{\pm}(T) = \mathcal{F}_{\pm}(T) - Td\mathcal{F}_{\pm}(T)/dT$. The critical temperature is that for which $\mathcal{F}_+(T_c) = \mathcal{F}_-(T_c)$, and the latent heat is defined as $L \equiv \rho_+(T_c) - \rho_-(T_c)$.

3.1 Bubble wall velocity and fluid profiles

For hydrodynamic considerations we can assume an infinitely thin wall (see, e.g., [35]), such that the temperature and the fluid velocity are discontinuous at the interface. Consider a stationary wall which is locally moving in the x direction. We call T_+ and T_- the temperatures just in front and just behind the wall, respectively. The continuity conditions for energy and momentum fluxes give the relations [45]

$$\begin{aligned} w_+ \gamma_+^2 v_+ &= w_- \gamma_-^2 v_-, & (21) \\ w_+ \gamma_+^2 v_+^2 + p_+ &= w_- \gamma_-^2 v_-^2 + p_-, & (22) \end{aligned}$$

where v_{\pm} are the values of the fluid velocity v on each side of the wall, in the rest frame of the wall, $\gamma = 1/\sqrt{1-v^2}$, $w = \rho + p$ is the enthalpy density, and we use the notation $p_+ \equiv p_+(T_+)$, $p_- \equiv p_-(T_-)$, etc. These equations give v_+ as a function of v_- . The solutions have two branches, called *detonations* and *deflagrations*. For detonations the incoming flow is faster than the outgoing flow ($|v_+| > |v_-|$). The value of $|v_+|$ is supersonic in all the range $0 < |v_-| < 1$, and has a minimum at the *Jouguet point* $|v_-| = c_s$, where the speed of sound c_s is given by $c_s^2(T) = \partial p / \partial \rho$. The minimum value of $|v_+|$ is called the Jouguet velocity v_j^{det} . For deflagrations we have $|v_+| < |v_-|$, and $|v_+|$ has a maximum value $v_j^{\text{def}} < c_s$ at the Jouguet point $|v_-| = c_s$. The hydrodynamical process is called *weak* if the velocities v_+ and v_- are either both supersonic or both subsonic. Otherwise, the hydrodynamical process is called *strong*.

There can also be discontinuities away from the phase-transition interface, which are called *shock fronts*. In this case Eqs. (21) and (22) still apply, only the equation of state relating the variables w , p , and T is the same on both sides of the discontinuity. As a consequence, the solution is simpler. The shock front is always supersonic.

A macroscopic equation for the friction force exerted by the plasma on the bubble wall is usually obtained by introducing a phenomenological damping term and then integrating

the equation of motion for the Higgs field. One obtains⁵ [36]

$$p_+ - p_- - \frac{1}{2}(s_+ + s_-)(T_+ - T_-) + \frac{\eta}{2}(|v_+|\gamma_+ + |v_-|\gamma_-) = 0, \quad (23)$$

where $s = w/T$ is the entropy density and η is the friction coefficient, which can be obtained from a microphysics calculation as explained in section 4. The various thermodynamical variables are not independent, so Eqs. (21), (22) and (23) have only four unknowns, namely, the velocities v_{\pm} and the temperatures T_{\pm} . Besides, the temperature T_+ can be determined from the temperature T_o outside the bubble, which is known from the dynamics of the phase transition (see below).

Out of the phase transition front, the fluid velocity profile (in the reference frame of the bubble center) depends on the symmetry of the bubble. This issue was discussed in Ref. [40]. The total amount of energy transmitted to the plasma is qualitatively and quantitatively similar for different wall geometries. We shall consider planar walls, which are simpler and allow to obtain analytical expressions (notice that, as bubbles collide, any previous symmetry is lost). For a stationary wall moving with velocity v_w , there is no characteristic distance scale in the fluid equations. As a consequence, it is usual to assume the *similarity condition* [45], namely, that the temperature and velocity of the fluid depend only on $\xi = x/t$. For the planar symmetry case, we have for the fluid velocity (see e.g. [40])

$$\left[\left(\frac{\xi - v}{1 - \xi v} \right)^2 - c_s^2 \right] v' = 0, \quad (24)$$

where a prime indicates derivative with respect to ξ . This equation gives either constant solutions $v(\xi) = \text{const}$, or a “rarefaction wave” solution

$$v_{\text{rar}}(\xi) = \frac{\xi - c_s}{1 - \xi c_s}. \quad (25)$$

Similarly, the enthalpy profile is given by the equation

$$\frac{w'}{w} = \left(\frac{1}{c_s^2} + 1 \right) \frac{\xi - v}{1 - \xi v} \gamma^2 v', \quad (26)$$

which can be readily integrated if v is a constant or the rarefaction solution (25). The fluid velocity and temperature profiles are thus constructed with these solutions, using the matching conditions (21) and (22) and appropriate boundary conditions.

The usual boundary conditions consist of a vanishing fluid velocity far behind the moving wall (at the center of the bubble) and far in front of the wall, where information on the bubble has not arrived yet. We shall refer to the temperature far in front of the wall as the “outside” temperature T_o . The initial value of T_o is the temperature T_n at which the bubble nucleated, but T_o will change due to the adiabatic expansion of the universe or the presence of other bubbles. To be consistent with the similarity condition, however, T_o should be a constant $T_o = T_n$, so that the wall velocity would also be a constant. We

⁵See [42] for a discussion on the validity of this equation.

shall assume that T_o changes slowly enough to allow the wall to be always in stationary motion.

Three kinds of solutions for the wall velocity and fluid profiles are possible (for a recent discussion see [42]), namely, a weak detonation, a “traditional” weak deflagration, and a supersonic Jouguet deflagration. Let us denote \tilde{v}_\pm the fluid velocities just in front and behind the wall, i.e.,

$$\tilde{v}_\pm \equiv \frac{v_\pm + v_w}{1 + v_w v_\pm}. \quad (27)$$

The wall is at the position $\xi_w = v_w$. For the detonation solution, the wall is supersonic and the fluid in front of it is unperturbed. Therefore, the fluid velocity \tilde{v}_+ vanishes and we have $v_w = |v_+|$. It turns out that the detonation solution can only be weak or, as a limiting case, Jouguet. Behind the wall, the fluid velocity is a constant $v = \tilde{v}_-$ up to a point ξ_0 which lies between c_s and ξ_w . At $\xi = \xi_0$ the fluid velocity matches the rarefaction solution (25). Continuity implies

$$\xi_0 = \frac{\tilde{v}_- + c_s}{1 + \tilde{v}_- c_s}. \quad (28)$$

The rarefaction solution vanishes at $\xi = c_s$, and we have $v = 0$ for $\xi < c_s$. For the traditional deflagration solution, the fluid behind the wall is at rest, so $\tilde{v}_- = 0$ and $v_w = |v_-|$. Again, this solution can only be weak or, at most, Jouguet. Therefore, the wall is subsonic. The fluid velocity in front of the wall is a constant $v = \tilde{v}_+$ up to a shock front where the profile ends, at a point $\xi_{sh} > c_s$ determined by the shock discontinuity conditions (see below). Beyond the shock, the fluid is still unperturbed. Finally, the supersonic deflagration is a Jouguet deflagration. In this case, the condition $\tilde{v}_- = 0$ of the traditional deflagration is replaced by the Jouguet condition $v_- = -c_s$, and we have

$$\tilde{v}_- = (v_w - c_s)/(1 - v_w c_s). \quad (29)$$

The wall velocity is always supersonic and the fluid velocity behind the wall is given by the rarefaction solution (25) between c_s and ξ_w . In front of the wall the fluid velocity is a constant $v = \tilde{v}_+$ between ξ_w and ξ_{sh} . In the limit $\xi_w = c_s$, there is no rarefaction wave and the solution matches the traditional deflagration. As ξ_w increases, the shock front and the phase-transition front become closer. As ξ_w reaches the Jouguet detonation velocity v_J^{det} , the shock wave disappears and the solution matches the detonation.

Equations (21), (22), and (23) for the wall velocity, and Eqs. (25) and (26) for the profiles, can be solved once the equation of state (EOS) of the system is known. It is convenient to approximate the model by using the bag EOS

$$\mathcal{F}_+(T) = -a_+ T^4/3 + \varepsilon, \quad \mathcal{F}_-(T) = -a_- T^4/3, \quad (30)$$

which corresponds to having only radiation and vacuum energy in the symmetric phase, and only radiation in the broken-symmetry phase. This simplification allows to find analytical expressions for the solutions. In this model the latent heat is given by $L = 4\varepsilon$ and the speed of sound is a constant, $c_s = 1/\sqrt{3}$. It is customary to express the results as functions of the variable $\alpha \equiv \varepsilon/(a_+ T^4)$ (which gives the ratio of the vacuum energy

density to the energy density of radiation). As discussed in Ref. [37], for applications it is convenient to use the latent heat L instead of ε . Therefore, we define the parameters

$$\alpha_c = \frac{L}{4a_+T_c^4}, \quad \alpha_+ = \frac{L}{4a_+T_+^4}, \quad \alpha_o = \frac{L}{4a_+T_o^4}, \quad (31)$$

corresponding to the critical temperature T_c , the temperature just in front of the bubble wall T_+ , and the temperature far in front of the wall T_o . The solutions for the wall velocity and fluid profiles will depend only on α_c , α_o , and η/L . The temperature T_o is the boundary condition for the temperature profile. The corresponding enthalpy density is given by

$$w_o = \frac{4}{3}a_+T_o^4 = \frac{L}{3\alpha_o}. \quad (32)$$

The matching conditions relating the values of w_- , w_+ and w_o are given by Eq. (21) at the phase-transition discontinuity and the equivalent equation for the shock discontinuity.

Using the equation of state (30) in Eqs. (21) and (22) we obtain the relation between v_+ and v_- , which for this model depends only on the parameter α_+ [46],

$$v_+ = \frac{\frac{1}{6v_-} + \frac{v_-}{2} \pm \sqrt{\left(\frac{1}{6v_-} + \frac{v_-}{2}\right)^2 + \alpha_+^2 + \frac{2}{3}\alpha_+ - \frac{1}{3}}}{1 + \alpha_+}. \quad (33)$$

The plus sign corresponds to detonations and the minus sign to deflagrations. The friction equation can also be expressed in terms of v_+ , v_- , and α_+ ,

$$\frac{4v_+v_-\alpha_+}{1 - 3v_+v_-} - \frac{2}{3} \left(1 + \frac{s_-}{s_+}\right) \left(1 - \frac{T_-}{T_+}\right) + \frac{2\alpha_+\eta}{L} (|v_+|\gamma_+ + |v_-|\gamma_-) = 0, \quad (34)$$

with

$$\frac{s_-}{s_+} = \frac{a_-}{a_+} \left(\frac{T_-}{T_+}\right)^3 \quad \text{and} \quad \frac{T_-}{T_+} = \left[\frac{a_+}{a_-} \left(1 - \alpha_+ \frac{1 + v_+v_-}{1/3 - v_+v_-}\right)\right]^{1/4}. \quad (35)$$

The ratio a_-/a_+ is given by $a_-/a_+ = 1 - 3\alpha_c$. From Eqs. (33)-(35) we can find the velocities v_+ and v_- as functions α_+ . The relation between α_+ and α_o depends on the type of hydrodynamic solution. For detonations, the wall velocity is given by $v_w = -v_+$ and the temperature T_+ is just the outside temperature, hence $\alpha_+ = \alpha_o$. For deflagrations, the temperature T_+ is related to T_o through the matching conditions at the shock discontinuity, which for the bag EOS are given by

$$v_1v_2 = \frac{1}{3}, \quad \frac{v_1}{v_2} = \frac{3T_o^4 + T_+^4}{3T_+^4 + T_o^4}, \quad (36)$$

where v_1 is the velocity of the outgoing flow in the reference frame of the shock, and v_2 that of the incoming flow. In the frame of the bubble center, the fluid velocity in front of the shock vanishes. Hence, the shock velocity is given by $v_{\text{sh}} = -v_2$, and we obtain

$$v_{\text{sh}} = \frac{\tilde{v}_1}{3} + \sqrt{\left(\frac{\tilde{v}_1}{3}\right)^2 + \frac{1}{3}}, \quad (37)$$

where \tilde{v}_1 is the fluid velocity behind the shock. In the shock-wave region the fluid velocity is a constant. As a consequence, we have $\tilde{v}_1 = \tilde{v}_+$, which gives

$$\frac{v_+ - v_w}{1 - v_+ v_w} = \frac{\sqrt{3}(\alpha_o - \alpha_+)}{\sqrt{(3\alpha_o + \alpha_+)(3\alpha_+ + \alpha_o)}}. \quad (38)$$

For traditional deflagrations, we have $v_- = -v_w$, so Eq. (38), together with Eq. (33), can be used to obtain α_+ as a function of α_o . For Jouguet deflagrations, $v_- = -1/\sqrt{3}$ is fixed, so Eq. (33) alone gives v_+ as a function of α_+ , i.e., $v_+ = v_J^{\text{def}}(\alpha_+)$. In this case, Eq. (38) gives the wall velocity as a function of α_+ and α_o , and Eq. (34) can be used to eliminate α_+ .

There is in general a solution for any set of parameters. As a matter of fact, there can be more than one. In such a case, only one of them will be realized in the phase transition. This issue is discussed in Ref. [42], where the semi-analytical solutions of Eqs. (33)-(38) are compared with a numerical calculation [47]. As a general rule, the weak detonation is more stable than the Jouguet deflagration, and the latter is more stable than the traditional deflagration. As an example, we show in Fig. 1 the solutions that are realized as final stationary states, as a function of the friction, for the values of the parameters considered in Ref. [42]. For large values of the friction we have weak deflagrations. When

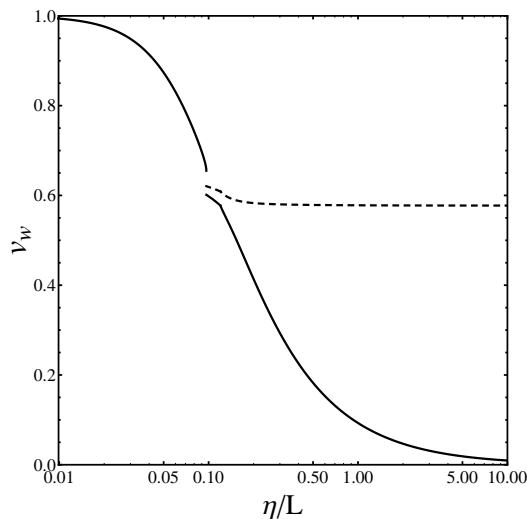


Figure 1: The wall velocity (solid line) and shock velocity (dashed line) as functions of the friction, for $\alpha_c = 4.45 \times 10^{-3}$ and $\alpha_o = 7.06 \times 10^{-3}$.

the speed of sound is reached, i.e., at the Jouguet point, the traditional deflagration matches the supersonic (Jouguet) deflagration (notice the discontinuity in the derivative of the curve, which is due to the change of hydrodynamical solution). For a lower value of the friction, the detonation solution appears. Since this solution is the stable one, there is a jump in the wall velocity as a function of η . The dashed line indicates the velocity of the shock front. We have $v_{\text{sh}} \simeq c_s$ for subsonic deflagrations.

3.2 Energy injected into the plasma

The energy released at the phase transition (i.e., the latent heat) reheats the plasma and causes bulk motions of the fluid. The generation of GWs requires the spherical symmetry to be lost. This happens once bubble walls or shock fronts collide. So far we have considered fluid profiles for stationarily moving walls, since it is hardly possible to know the profiles during bubble collisions. This is irrelevant for the envelope approximation, which only takes into account the motion of uncollided walls (and assumes thin profiles). To estimate the average energy which goes into the formation of turbulence, we may calculate the energy density of the fluid just before the profiles meet, and assume that, after the fronts collide, this energy gets redistributed throughout the space occupied by the bubbles. With this assumption, we only need to consider the average energy density for isolated bubbles. Notice that, although there are bubbles of different sizes (because they nucleated at different times), the wall velocities and fluid profiles depend only on the temperature T_o (which is the same for all bubbles).

The kinetic energy density of the fluid is given by $\rho_{\text{kin}} = wv^2\gamma^2$. Let us first consider the subsonic deflagration. For planar walls, the kinetic energy density is a constant between the wall and the shock front, $\rho_{\text{kin}} = w_+\tilde{v}_+^2\tilde{\gamma}_+^2$, and vanishes elsewhere. Therefore, the total energy is proportional to $R_{\text{sh}} - R_b$, where R_b and R_{sh} are the positions of the bubble and the shock front, respectively. To calculate these positions we should integrate the respective velocities. However, the profiles were calculated using the similarity condition and, for consistency, we must consider again this approximation⁶. Thus, we have $R_b = \xi_w\Delta t_b$, $R_{\text{sh}} = \xi_{\text{sh}}\Delta t_b$, where Δt_b is the time during which the wall has been moving, ξ_w is the wall velocity calculated from Eqs. (33)-(38) and ξ_{sh} is the shock front velocity given by Eq. (37). Assuming that, after the shock fronts meet, the energy which was initially concentrated in front of the bubble wall gets distributed in the whole volume proportional to $\xi_{\text{sh}}\Delta t_b$, the average kinetic energy density in the fluid is given by

$$\rho_K = w_+\tilde{v}_+^2\tilde{\gamma}_+^2\frac{\xi_{\text{sh}} - \xi_w}{\xi_{\text{sh}}} \quad (\text{subsonic deflagrations}), \quad (39)$$

which is the same for bubbles nucleated at different times.

For detonations, the kinetic energy density is concentrated between c_s and ξ_w . Between c_s and ξ_0 there is the rarefaction wave, and between ξ_0 and ξ_w the fluid profiles are constant. The integration of the kinetic energy density in the rarefaction region was done analytically in Ref. [40]. In the case of detonations, bubble collisions and turbulence begin when the bubble walls meet (since there are not shock fronts). Dividing the total kinetic energy by the volume of the bubble, we have

$$\rho_K = w_- \left[\tilde{v}_-^2\tilde{\gamma}_-^2\frac{\xi_w - \xi_0}{\xi_w} + \frac{3}{4} \left(2 - \sqrt{3}\right)^{\frac{2}{\sqrt{3}}} \left(\frac{1 - \tilde{v}_-}{1 + \tilde{v}_-}\right)^{\frac{2}{\sqrt{3}}} \frac{f(\xi_w) - f(c_s)}{\xi_w} \right] \quad (\text{detonations}), \quad (40)$$

where

$$f(\xi) = \left(\frac{1 + \xi}{1 - \xi}\right)^{\frac{2}{\sqrt{3}}} \left\{ \frac{2}{\sqrt{3}} - 1 + (1 - \xi) \left[2 - {}_2F_1\left(1, 1, \frac{2}{\sqrt{3}} + 1, \frac{1 + \xi}{2}\right) \right] \right\}, \quad (41)$$

⁶Our numerical calculation shows that the velocity generally varies by at most a 30% before colliding.

and ${}_2F_1$ is the hypergeometric function.

The profile of a supersonic deflagration consists of a shock wave in front of the wall and a rarefaction wave behind it. The average kinetic energy density is thus given by

$$\rho_K = w_- \frac{3}{4} \left(\frac{1 - \xi_w}{1 + \xi_w} \right)^{\frac{2}{\sqrt{3}}} \frac{f(\xi_w) - f(c_s)}{\xi_{sh}} + w_+ \tilde{v}_+^2 \tilde{\gamma}_+^2 \frac{\xi_{sh} - \xi_w}{\xi_{sh}} \quad (\text{supersonic deflagrations}). \quad (42)$$

3.3 Bubble nucleation, expansion and percolation

In principle, as soon as the temperature descends below T_c , bubbles begin to nucleate and expand. However, at the beginning there will be too few bubbles. The “onset” of nucleation is usually defined as the time at which there is already one bubble in a Hubble volume. We shall take this as the nucleation time of the “first” bubbles. These will be the largest bubbles in the system, thus setting the characteristic wavelength of the GWs.

On the other hand, bubble collisions can in principle begin as soon as there is a non-vanishing probability of having a couple of bubbles in a causal volume. However, at the beginning the bubbles will be too few and too small, hence their collisions will be very unlikely. Bubbles will effectively begin to meet and collide once their density and size have become large enough. At first, there will form clusters of a few bubbles, and then larger and larger clusters. Percolation occurs when a cluster of infinite size spreads through the medium (equivalently, when there is a cluster spreading from side to side in a large box, say, of Hubble size). Percolation has been studied numerically for spheres (of equal size) in a large box. With the spheres distributed at random and allowing overlapping, an infinite chain is established when the fraction of space covered by spheres is 0.29 [48]. We shall assume that, at this moment, most bubbles are already colliding.

The nucleation of bubbles [49, 50] is governed by the three-dimensional instanton action

$$S_3 = 4\pi \int_0^\infty r^2 dr \left[\frac{1}{2} \left(\frac{d\phi}{dr} \right)^2 + V_T(\phi(r)) \right], \quad (43)$$

where

$$V_T(\phi) \equiv \mathcal{F}(\phi, T) - \mathcal{F}(0, T). \quad (44)$$

The bounce solution of this action, which is obtained by extremizing S_3 , gives the radial configuration of the nucleated bubble, assumed to be spherically symmetric. The action of the bounce coincides with the free energy of a critical bubble in unstable equilibrium between expansion and contraction. The solution obeys the equation

$$\frac{d^2\phi}{dr^2} + \frac{2}{r} \frac{d\phi}{dr} = \frac{dV_T}{d\phi}, \quad (45)$$

with boundary conditions

$$\frac{d\phi}{dr}(0) = 0, \quad \lim_{r \rightarrow \infty} \phi(r) = 0. \quad (46)$$

The thermal tunneling probability for bubble nucleation per unit volume per unit time is [50]

$$\Gamma(T) \simeq A(T) e^{-S_3(T)/T}, \quad (47)$$

with $A(T) = [S_3(T)/(2\pi T)]^{3/2} T^4$. At the critical temperature, S_3 diverges and the nucleation rate vanishes, whereas at the temperature at which the barrier between the minima of \mathcal{F} disappears, S_3 vanishes and the nucleation rate becomes extremely high, $\Gamma \sim T^4$.

We define the nucleation time t_i of the first bubbles by the condition

$$V_H n(t_i) = 1, \quad (48)$$

where $V_H = H^{-3}$ is the Hubble volume, and the number density of bubbles is given by

$$n(t) = \int_{t_c}^t dt' \Gamma(T(t')) \left[\frac{a(t')}{a(t)} \right]^3, \quad (49)$$

where t_c is the time at which the Universe reached the critical temperature T_c . The scale factors take into account the fact that bubbles which nucleated at time t' with a number density $dt' \Gamma(T(t'))$, get diluted until time t due to the expansion of the Universe. At this initial stage, the temperature variation is determined by the adiabatic expansion equation $d\rho_+ = -3w_+ da/a$. Hence, we have

$$dT = -3 \frac{d\mathcal{F}_+/dT}{d^2\mathcal{F}_+/dT^2} \frac{da}{a}. \quad (50)$$

The evolution of the scale factor is given by the Friedmann equation

$$\frac{da}{a} = H dt, \quad (51)$$

with the expansion rate given by

$$H = \sqrt{8\pi G \rho_+ / 3}. \quad (52)$$

If the high-temperature phase is comprised only of radiation and vacuum energy, then Eq. (50) becomes $dT = -T da/a$, which gives the well known result $dT/dt = -HT$. However, some of the models we consider in the next section have particles with masses $\sim T$ in the + phase.

When bubbles begin to nucleate, the energy density is no longer homogeneous. On the one hand, even if the temperature were homogeneous, the internal energy of the - phase is lower than that of the + phase. On the other hand, temperature gradients arise due to the latent heat released at the interfaces. The Hubble rate is thus governed by the average energy density. In fact, energy conservation implies that the released energy compensates the decrease in the broken-symmetry phase. As a consequence, the average energy density will not depart significantly from $\rho_+(T_o)$, which decreases due to the adiabatic expansion. Therefore, we shall use Eq. (52) still in the presence of bubbles. This is a good approximation for the stages of the phase transition we are interested in (i.e., up to the percolation time). In any case, the scale factor will not change significantly during the inhomogeneous stage. We have checked numerically that, as soon as the broken-symmetry regions become barely appreciable, say, at a time t when the fraction of volume occupied by bubbles reaches a value $f_b \sim 10^{-2}$, the phase transition

is already happening so quickly (due to the extreme behavior of the nucleation rate) that the percolation fraction $f_b \simeq 0.3$ is achieved in a time $\delta t \ll t - t_c$.

Assuming a homogeneous nucleation throughout the symmetric-phase regions, the fraction of volume occupied by bubbles is $f_b = 1 - f_u$, where f_u is the fraction of space in the unbroken-symmetry phase, given by [51]

$$f_u(t) = \exp \left[-\frac{4\pi}{3} \int_{t_c}^t dt' \Gamma(T_o') \left(\frac{a'}{a} \right)^3 R_b(t', t)^3 \right]. \quad (53)$$

The radius of a bubble that nucleated at time t' and expanded until time t is given by

$$R_b(t', t) = R_n(T_o') \frac{a}{a'} + \int_{t'}^t v_w(T_o'') \frac{a}{a''} dt'', \quad (54)$$

where R_n is the initial radius of the nucleated bubble, which immediately becomes negligible in comparison to the second term in Eq. (54). We have used the notation $T_o' = T_o(t')$, $a' = a(t')$, etc. Notice that, at a given time t , all bubble walls move with velocity $v_w(T_o(t))$, where $T_o(t)$ evolves according to Eq. (50). We shall assume that, as the temperature decreases, the hydrodynamics instantaneously adjusts to a stationary solution. Moreover, if the stable type of stationary solution changes, e.g., from a deflagration to a detonation, we approximate the velocity variation by a jump. The factors of a in Eqs. (53) and (54) take into account the fact that the number density of nucleated bubbles gets diluted and the radius of a bubble gets stretched due to the expansion of the Universe from t' to t . The exponent in Eq. (53) would give a naive result for f_b assuming a homogeneous nucleation rate throughout space (including the broken-symmetry regions). Thus, Eq. (53) avoids overcounting of overlapping or nested bubbles. This result is obtained by considering the probability that a given point in space lies outside of any bubble (this is why a bubble that nucleated in the broken-symmetry region does not contribute to f_b even though it contributes to the exponent).

However, Eq. (53) assumes that the nucleation is homogeneous in the symmetric phase, with a rate $\Gamma(T_o)$. In fact, temperature profiles may cause considerable inhomogeneities in the nucleation rate. Consider bubbles which have not yet interacted with each other. If the hydrodynamic solution is a detonation, then the temperature in the symmetric phase is just $T = T_+ = T_o$, and Eq. (53) does indeed hold. On the other hand, in the case of deflagrations there is a reheated zone in front of the bubble walls ($T_+ > T_o$). Since the nucleation rate is extremely sensitive to temperature, bubble nucleation is effectively turned off in such regions. Therefore, we can assume that the nucleation rate vanishes, not only inside the bubbles, but also in the shock-wave regions, whereas it is given by $\Gamma(T_o)$ beyond the shock fronts. Equation (53) does not take into account this fact, and must be modified in order to avoid bubble overcounting. We accomplish this by considering, instead of f_b , the fraction of volume f_{sh} occupied by ‘‘shock-front bubbles’’, which is obtained by **replacing the bubble radius R_b in Eq. (53) by the shock front radius R_{sh}** calculated from the shock front velocity v_{sh} instead of v_w . Moreover, in the deflagration case we are not interested in f_b but in f_{sh} , since turbulence begins as soon as the shocks collide.

We shall follow the evolution of the phase transition up to the percolation time t_p , which we define as the moment at which the fraction of volume occupied by bubbles (in

the case of detonations) or by *shock bubbles* (in the case of deflagrations) reaches the value 0.3. We will solve Eq. (45) iteratively by the overshoot-undershoot method, and we will integrate Eq. (43), Eq. (49), and the set of Eqs. (50)-(54) numerically (see Ref. [26] for details). The relevant quantities, such as the temperature $T(t_p)$ or the size of the bubbles (which roughly goes with $t_p - t_i$) are not much sensitive to the definitions of t_i and t_p . Indeed, these definitions involve the bubble number density n and the fractions of volume f_b or f_{sh} which, due to the extreme behavior of Γ with t , change by many orders of magnitude in the characteristic time $t_p - t_i$. As a consequence, changing the values of n or f that one uses to define t_i and t_p (even by an order of magnitude) introduce very small differences $\Delta t_{i,p} \ll t_{i,p}$. We have checked this issue numerically.

In order to compute the GW signal from bubble collisions, we only need to evaluate the wall velocity, the kinetic energy of the fluid, and the parameter β defined in Eq. (11). Since the dynamics of nucleation is dominated by the variation of S_3 , we can neglect the variation of the prefactor in Eq. (47). Therefore, we have

$$\frac{\beta}{H} = T \frac{d(S_3/T)}{dT}. \quad (55)$$

This parameter must be computed at some characteristic temperature. It is not clear whether this temperature should be chosen close to T_i or rather to the later temperature T_p . In the simulation which gives the fit (9)-(10), β is a constant [27]. In Fig. 2 we show the values of β both at the initial time and at the percolation time for one of the models considered in the next section. We see that the difference is a factor of $\mathcal{O}(1)$ (generally less than 2), except for extremely strong phase transitions (which are those very close to the maximum value of the parameter h_s in Fig. 2). In general, this difference⁷ is quite smaller than other uncertainties (see below), and we shall use the value $\beta(T_i)$.

In Fig. 2 we also show the value of S_3/T at T_i and T_p . We see that $S_3(T_i)/T_i$ takes values around the well known estimation $S_3/T \sim 140$, which can be deduced from Eqs. (18)-(20). Notice also that the value of β departs in general from the usual assumption $\beta \sim 100H$. This assumption is based on the argument that the time scale for change in the nucleation action should be comparable to that in which the temperature changes [16], which gives $\beta/H \sim S_3/T$. We see that this estimate is too crude. We also see that the approximation $\Delta t \approx 3 \log(\beta/H)\beta^{-1}$ gives a very good estimate of the time $\Delta t = t_p - t_i$. In contrast, the estimation $\Delta t \approx \beta^{-1}$ is at least an order of magnitude smaller than Δt .

In order to compute the contribution of turbulence to the generation of gravitational waves, we shall calculate the average energy density in bulk motions of the plasma at the percolation time. We also need to know the typical size of the bubbles. As discussed in section 2, there is an arbitrariness in the appropriate size scale L_s , and we shall consider the largest bubbles. We shall calculate the radius $R_b(t_i, t_p)$ of the largest bubbles in the case of detonations, or the radius $R_{sh}(t_i, t_p)$ of the largest shock-front bubbles in the case of deflagrations, by integrating the corresponding velocity v_w or v_{sh} from t_i to t_p . Regarding the widely used approximation $R_b \approx v_w \beta^{-1}$ for the largest bubbles, as we have seen, $R_b \approx v_w 3 \log(\beta/H) \beta^{-1}$ will give a much better approximation. In Fig. 3 we show the

⁷The difference between $\beta(T_i)$ and $\beta(T_p)$ becomes larger near the maximum value of h_s . However, for very strong phase transitions it is convenient to evaluate β at T_i since this parameter may become negative for small temperatures (see, e.g., Fig. 5 of Ref. [22]).

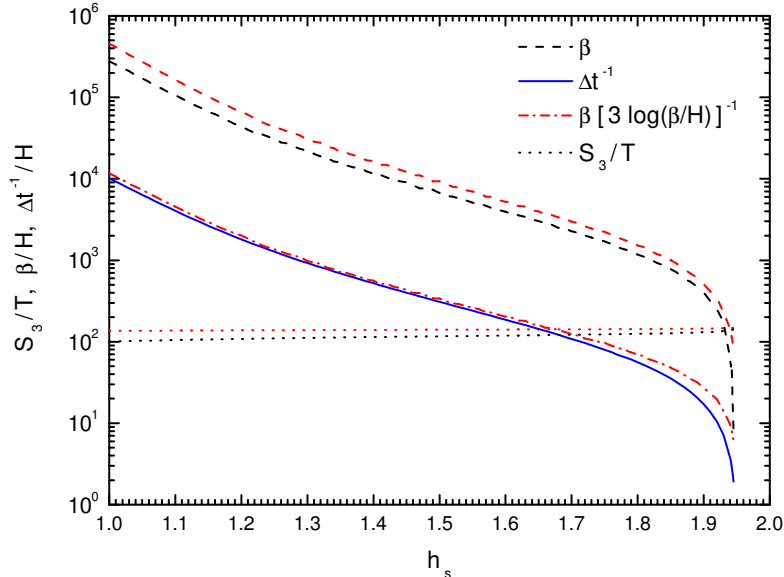


Figure 2: The inverse time scales and the bounce action, for an extension of the SM with a complex scalar singlet with coupling h_s to the Higgs and invariant mass $\mu_s = 0$. Red lines are calculated at $t = t_i$, black lines at $t = t_p$, and the blue line corresponds to $t_p - t_i$.

largest bubble radius at the percolation time, together with the two estimations. For this particular example, the approximation $\Delta t = \beta^{-1}$ underestimates the radius by a factor ≈ 30 in most of the parameter range considered in the figure. Hence, this approximation will underestimate the amplitude of the waves by a factor ≈ 900 . Figure 3 also shows that considering a constant velocity $v_w = v_w(T_i)$ is in general a good approximation, as well as $\beta = \beta(T_i)$.

4 The electroweak phase transition

In the SM, the electroweak phase transition is only a smooth crossover [33]. However, many extensions of the model give a first-order phase transition. For simplicity we shall consider models with a single Higgs field, or models for which a single Higgs provides a good approximation.

4.1 Effective potential and bag parameters

Our theory will consist of a tree-level potential

$$V_0(\phi) = -m^2\phi^2 + \frac{\lambda}{4}\phi^4 \quad (56)$$

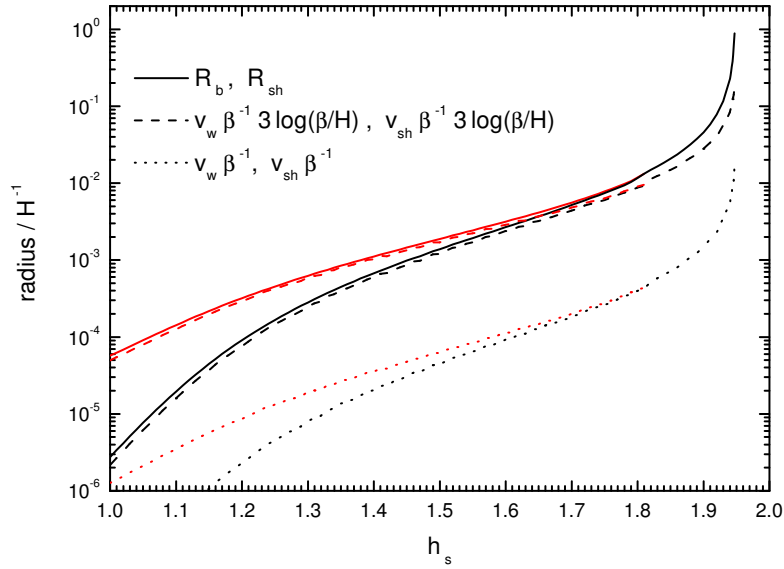


Figure 3: The radius of the largest bubbles at $t = t_p$ and the different approximations, for the same model and parameters of Fig. 2. Black lines correspond to the bubble wall and red lines to the shock wall. The parameter β is calculated at the initial temperature T_i .

for the background Higgs field ϕ , defined by $\langle H^0 \rangle \equiv \phi/\sqrt{2}$. The vacuum expectation value (vev) of ϕ is given by $v = \sqrt{2/\lambda} m = 246 \text{ GeV}$, and λ fixes the Higgs mass, $m_H^2 = 2\lambda v^2$. Imposing the renormalization conditions that the minimum of the potential and the mass of ϕ do not change with respect to their tree-level values [52], the one-loop zero-temperature effective potential is given by $V(\phi) = V_0(\phi) + V_1(\phi)$, with

$$V_1(\phi) = \sum_i \frac{\pm g_i}{64\pi^2} \left[m_i^4(\phi) \left(\log \left(\frac{m_i^2(\phi)}{m_i^2(v)} \right) - \frac{3}{2} \right) + 2m_i^2(\phi)m_i^2(v) \right] + c, \quad (57)$$

where the upper and lower signs correspond to bosons and fermions, respectively, g_i is the number of d.o.f. of the particle species i , $m_i(\phi)$ is the ϕ -dependent mass, and the constant c is chosen so that the energy density vanishes in the true vacuum at zero temperature [37], $V_0(v) + V_1(v) = 0$. The free energy (finite-temperature effective potential) to one-loop order, including the resummed daisy diagrams, is given by

$$\mathcal{F}(\phi, T) = V_0(\phi) + V_1(\phi) + \mathcal{F}_1(\phi, T), \quad (58)$$

where the finite-temperature corrections are given by [53]

$$\begin{aligned} \mathcal{F}_1(\phi, T) &= \sum_i \pm \frac{g_i T^4}{2\pi^2} \int_0^\infty dx x^2 \log \left[1 \mp \exp \left(-\sqrt{x^2 + m_i^2(\phi)}/T \right) \right] \\ &+ \sum_{\text{bosons}} \frac{g_i T}{12\pi} [m_i^3(\phi) - \mathcal{M}_i^3(\phi)]. \end{aligned} \quad (59)$$

Here, \mathcal{M}_i is given by $\mathcal{M}_i^2(\phi) = m_i^2(\phi) + \Pi_i(T)$, where $\Pi_i(T)$ is the thermal mass. The last term receives contributions from all the bosonic species except the transverse polarizations of the gauge bosons. Some of the masses in the gauge sector are gauge dependent. We use the Landau gauge and, thus, we consider only the transverse and longitudinal polarizations of the gauge bosons⁸.

We shall consider in general Higgs-dependent masses of the form

$$m_i^2(\phi) = h_i^2 \phi^2 + \mu_i^2. \quad (60)$$

For $\mu_i \ll T$, the contribution of the species i to the energy density of the unbroken-symmetry phase is that of radiation, i.e., proportional to $g_i T^4$. Since this is true for most species, we have in general $\rho_+ \approx \pi^2 g_* T^4/30 + \rho_{\text{vac}}$, where g_* is the number of relativistic d.o.f., and $\rho_{\text{vac}} = V_0(0) + V_1(0)$ is the false vacuum energy density. In such a case, the bag parameters are given by $a_+ = \pi^2 g_*/30$ and $\epsilon = \rho_{\text{vac}}$. In the general case, we define the *thermal* energy density by $\rho_+^{\text{th}} = \rho_+ - \rho_{\text{vac}}$ and compute the bag parameters α_c, α_o , etc., by

$$\alpha(T) = \frac{L}{4\rho_+^{\text{th}}(T)}, \quad (61)$$

where the latent heat is given by $L = T_c (d\mathcal{F}_-/dT - d\mathcal{F}_+/dT)|_{T_c}$ (which does not fulfil in general the bag relation $L = 4\epsilon$).

⁸Although physical quantities such as the latent heat or the amount of supercooling should not exhibit any gauge dependence, an inconsistent truncation of the perturbative expansion can introduce a nontrivial gauge dependence [54]. This would be important in a model for which the strength of the phase transition relies on the gauge fields, which is not the case of the models considered here.

4.2 Friction force

The friction was calculated in several studies of the microphysics [55, 56]. Some general approximations were derived in Refs. [25, 37]. The friction coefficient appearing in Eq. (23) receives contributions from *thermal particles*, i.e., those which obey the Boltzmann equation, and from *infrared bosons*, i.e., infrared excitations of bosonic fields, which must be treated classically. For masses of the form (60) we have, for thermal particles,

$$\eta_{\text{th}} = \sum_i \frac{g_i h_i^4}{\bar{\Gamma}/T} T \int_0^{\phi_c} [c_1(m_i/T)]^2 (\phi/T)^2 \sqrt{2V_T} d\phi, \quad (62)$$

where V_T is defined in Eq. (44), the limits of integration correspond to the minima of the free energy at $T = T_c$, the function c_1 is given by

$$c_1(x) = \frac{1}{2\pi^2} \int_x^\infty dy \sqrt{y^2 - x^2} \frac{e^y}{(e^y \mp 1)^2}, \quad (63)$$

and $\bar{\Gamma}$ is an average interaction rate arising from the collision term of the Boltzmann equation. For the electroweak phase transition, $\bar{\Gamma}$ is typically $\sim 10^{-2}$. For infrared bosons, we have

$$\eta_{\text{ir}} = \sum_{\text{bosons}} \frac{g_i h_i^4 \pi m_D^2}{8T^2} T \int_{\phi_0}^{\phi_c} b(m_i/T) (\phi/T)^2 \sqrt{2V_T} d\phi, \quad (64)$$

where m_D is the Debye mass, given by $m_D^2 = (11/6)g^2T^2$ for the W and Z bosons of the SM, and $m_D^2 = h^2T^2/3$ for a scalar singlet. The integral in (64) has an infrared cut-off ϕ_0 for small μ_i , given by $\phi_0 = \sqrt{L_w^{-2} - \mu_i^2}/h$ for $\mu_i < L_w^{-1}$, and $\phi_0 = 0$ for $\mu_i > L_w^{-1}$, where L_w is the wall width. In the thin wall approximation, L_w can be estimated as $L_w \approx \int_{0.1\phi_c}^{0.9\phi_c} d\phi/\sqrt{2V_T}$. The function b is given by

$$b(x) = \frac{1}{2\pi^2} \int_x^\infty \frac{dy}{y^3} \frac{e^y}{(e^y - 1)^2}. \quad (65)$$

Each of these two contributions dominates in different parameter regions, and we can use $\eta = \eta_{\text{th}} + \eta_{\text{ir}}$. Analytical approximations for η_{th} and η_{ir} in different limits can be found in Ref. [37].

The above expressions for the friction coefficient were derived in the small-velocity regime. Recently, the ultra-relativistic regime was considered in Ref. [39]. In this limit the friction does not depend on the velocity. The total force per unit area acting on a wall which is already propagating ultra-relativistically (with gamma factor $\gamma \sim 10^9$) is given by

$$F_{\text{tot}}/A = \tilde{p}_- - \tilde{p}_+ = -\tilde{\mathcal{F}}_- + \tilde{\mathcal{F}}_+, \quad (66)$$

where $\tilde{\mathcal{F}}(\phi, T)$ is the-mean field effective potential. The latter is obtained by keeping only the quadratic terms in a Taylor expansion of the finite-temperature part of $\mathcal{F}(\phi, T)$ about $\phi = 0$ [39, 38],

$$\tilde{\mathcal{F}}(\phi, T) = V_0(\phi) + V_1(\phi) + \sum_i [m_i^2(\phi) - m_i^2(0)] \frac{d\mathcal{F}_1}{dm_i^2} \Big|_{\phi=0}. \quad (67)$$

For the case of bosons with masses of the form $m_i = h_i\phi$ (i.e., $\mu_i = 0$, which gives stronger phase transitions), the last term in Eq. (67) becomes

$$\sum_i \frac{g_i h_i^2}{24} T^2 \phi^2. \quad (68)$$

For fermions there is an additional factor $1/2$.

If the total force (66) is positive, then the wall can run away. This means that the bubble may undergo accelerated expansion instead of reaching one of the stationary states considered in the previous section. As shown in Ref. [39], the bubble wall never runs away in a “fluctuation induced” first-order phase transition, i.e., a phase transition which is first-order due to the thermal part of the potential. The typical example of a fluctuation-induced first-order phase transition occurs when the high-temperature expansion of $\mathcal{F}_1(\phi, T)$ has a cubic term $-\sum_i T m_i^3(\phi)/12\pi$. This term is not present in the mean field potential. If the first-order character of the phase transition is due to this term alone, then in the mean field potential the broken symmetry minimum raises above the symmetric minimum. As a consequence, the force (66) is negative, which means that the wall cannot run away. An example of a model which may yield a strong enough first-order phase transition is a potential with tree-level cubic terms [39]. This is possible, e.g., in extensions of the Standard Model with singlet scalar fields.

5 Numerical results

The relevant SM contributions to the one-loop effective potential come from the Z and W bosons, the top quark, and the Higgs and Goldstone bosons. It is usual to ignore the Higgs sector in the one-loop radiative corrections. This should be a good approximation in extensions of the SM which include particles with strong couplings to ϕ . The ϕ -dependent masses of the weak gauge bosons and top quark are of the form $h_i\phi$, with $h_i = m_i/v$, where m_i are the physical masses at zero temperature. We shall ignore the longitudinal components of the weak gauge bosons, which are screened by plasma effects. Thus, the W and Z contribute corrections of the form (57),(59), with 4 and 2 bosonic d.o.f., respectively. The top contributes $g_t = 12$ fermionic d.o.f. The rest of the SM particles have $h_i \ll 1$ and only contribute a ϕ -independent term $-\pi^2 g_{\text{light}} T^4/90$, with $g_{\text{light}} \approx 90$. We shall consider several extensions of the SM, which may provide a strongly first-order phase transition. For all the models considered below, we use a Higgs mass $m_H = 125$ GeV. The dependence of the relevant quantities on the strength of the phase transition is illustrated in Fig. 4. For further results on the wall velocity for these models, see Ref. [37]. For Results on the temperature and duration of the different stages of the phase transition, see Ref. [26]. In this paper we shall focus on the gravitational waves generated during the phase transition.

5.1 Extra scalars

The simplest extension of the SM consists of adding gauge singlet scalars [52, 57], which may range from a single field S [58, 59, 60] to several fields S_i [61]. In general, these bosons

constitute a hidden sector which couples only to the SM Higgs doublet through a term $h_s^2 H^\dagger H \sum S_i^2$ (assuming, for simplicity, universal couplings $h_i = h_s$). The scalars may have $SU(2) \times U(1)$ invariant mass terms $\mu_s^2 S^2$ and quartic terms $\lambda_s S^4$. For simplicity, we shall set $\lambda_s = 0$ for our numerical calculations. We have checked that considering $\lambda_s \neq 0$ does not introduce qualitative differences in the results. A negative value of μ_s^2 may enhance the strength of the phase transition. This fact is exploited in the case of the MSSM in the light-stop scenario, which we consider in the next subsection. Besides, adding real singlets allows cubic terms of the form $(H^\dagger H) S$ or S^3 , which cannot be constructed with Higgs doublets. The presence of cubic terms in the tree-level potential makes it easier to get a strongly first-order electroweak phase transition [58]. This may cause a significant increase in the wall velocity [37] and even the existence of runaway solutions [39]. As a consequence, tree-level effects may lead to an important GW signal from bubble collisions [9]. In order to study such tree-level effects, one should consider the full potential depending on the two fields H and S . This is out of the scope of the present paper, since our numerical calculations are based on a single-variable potential $V(\phi)$. Therefore, we shall ignore the possibility that cubic terms exist in the tree-level potential. Thus, the contributions of the scalars to the free energy are of the form (57),(59), with $m_s^2(\phi) = h_s^2 \phi^2 + \mu_s^2$ and g_s given by the number of real singlets. The thermal mass is given by $\Pi = h_s^2 T^2/3$ [59].

It is well known that the phase transition is more strongly first-order for larger numbers of bosons g_s and stronger couplings h_s (see Fig. 4). On the contrary, for high values of μ_s the bosons decouple from the thermal plasma, and the phase transition becomes more weakly first-order. As a consequence, the wall velocity and the energy injected into macroscopic motions of the fluid generally grow with g_s and h_s and decrease with μ_s . Indeed, increasing g_s and h_s , the separation between minima of the free energy increases, as well as the height of the barrier separating them. As a consequence, bubble nucleation effectively begins at lower temperatures T_i [22, 26]. For this particular model, the strength of the first-order phase transition has a strong dependence on the coupling h_s . For large enough values of h_s there is a barrier at zero temperature, and the nucleation temperature T_i is very small. As shown in Fig. 4, there is a value $h_s = h_{\max}$ for which T_i falls to 0 (upper left panel). Beyond this value the phase transition is too strong to overcome the supercooling stage and the Universe will eventually enter a period of inflation [22, 26]. This is reflected also in Figs. 2 and 3. The endpoint in the curves corresponds to h_{\max} . Near this endpoint, the system remains stuck in the symmetric phase for a long time $t_i - t_c \gg H^{-1}$ (upper right panel of Fig. 4). Meanwhile, the temperature decreases to a value $T_i \ll T_c$. The same happens to the time $\Delta t = t_p - t_i$ needed to arrive at percolation, as can be seen in Fig. 2.

The generation of gravitational waves depends mainly on the wall velocity and the kinetic energy in bulk motions of the fluid. We show the values of these quantities at $t = t_i$ in the lower panels of Fig. 4. The behavior at the percolation time is similar. We can distinguish a cusp in these curves, which indicates the passage from a value of h_s for which the hydrodynamical solution is a weak deflagration, to a value of h_s for which the wall moves as a Jouguet deflagration. Similarly, there is a jump indicating the passage from a Jouguet deflagration to a weak detonation. Notice that, although the wall velocity for the detonation is higher at the discontinuity point, the detonation is a weaker

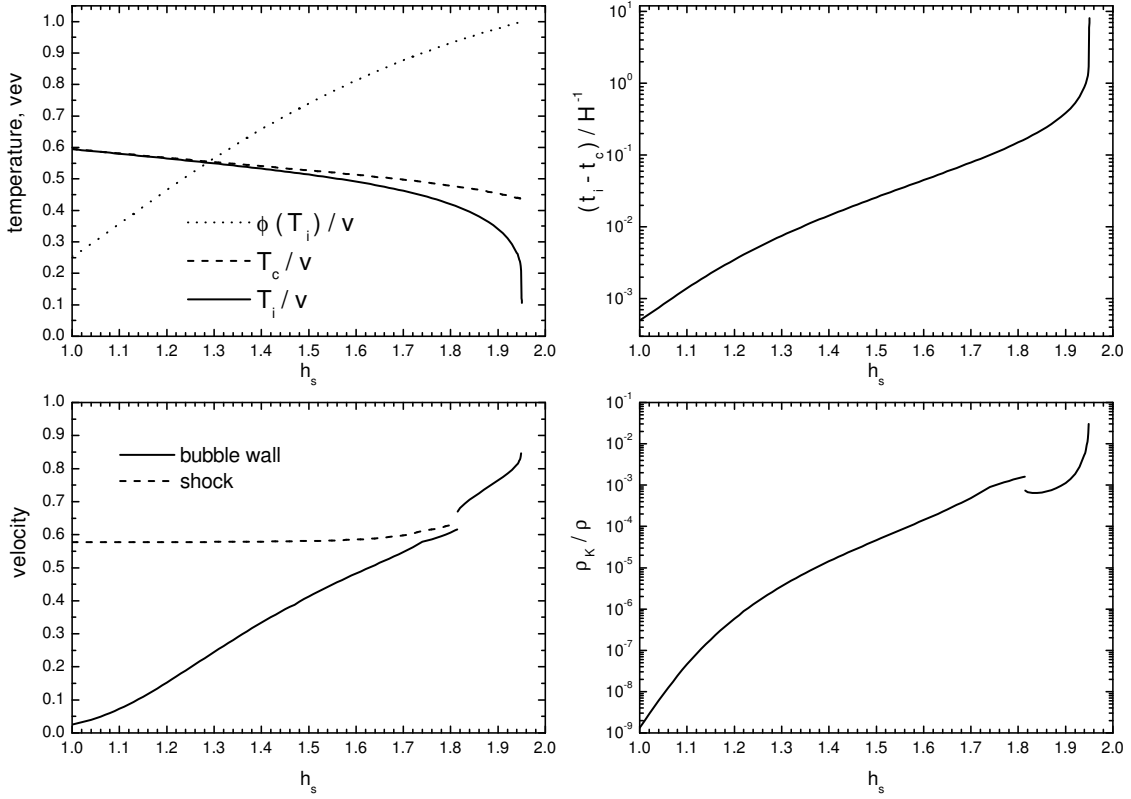


Figure 4: Several quantities calculated at the beginning of bubble nucleation, as functions of h_s for $g_s = 2$ and $\mu_s = 0$: the temperature and field mean value (upper left), the supercooling time $t_i - t_c$ (upper right), the bubble wall and shock velocities (lower left), and the kinetic energy of the fluid (lower right).

hydrodynamical solution than the supersonic deflagration and causes a lower disturbance of the fluid. Therefore, the jump in the injected kinetic energy is negative. The local maximum at this discontinuity is due to the fact that the kinetic energy is maximal for Jouguet deflagrations [38, 40].

This behavior is reflected in the gravitational wave generation, as can be seen in Figs. 5, 6 and 7. In Fig. 5 we plot the peak of the GW spectrum from turbulence, as a function of h_s for different values of g_s and μ_s . As the parameters of the model are varied, the peak frequency and intensity change by several orders of magnitude. This variation includes frequencies in the sensitivity range of LISA and eLISA, $f \sim 1$ mHz. However, the peak sensitivity of LISA, $h^2\Omega_{\text{GW}} \sim 10^{-12}$, and that of eLISA, $h^2\Omega_{\text{GW}} \sim 10^{-10}$ (marked with horizontal dotted lines in Fig. 5), are reached near the maximum values of h_s . Unfortunately, for such high intensities the spectra do not peak at mHz frequencies. For values of h_s which give mHz frequencies, the intensities are a few orders of magnitude below LISA's sensitivity. This is better seen in Fig. 6, where the peak value Ω_p is shown as a function of the peak frequency f_p , together with the sensitivity curves⁹ for LISA and eLISA. The curves for the predicted signal cross LISA's sensitivity curve at $f_p \sim 10^{-4}$ Hz. This happens very close to the endpoints. Reaching LISA's sensitivity thus requires to tune the coupling h_s close to h_{max} at least at the 1% level. The GW signals do not reach the sensitivity curve for eLISA, even for the strongest phase transitions.

We find that the signal from bubble collisions is much weaker than that from turbulence. As an example, we plot the case $g_s = 2$, $\mu_s = 0$ in Fig. 7. The spectrum from bubble collisions peaks at a higher frequency. Therefore, bubble collisions will cause a secondary peak in the total GW spectrum. However, this peak cannot be observed by LISA. For comparison, we show in Fig. 6 the peak signals from turbulence and bubble collisions for some values of h_s which give a sizeable signal. This result agrees with Ref. [22], where only the signal from bubble collisions was considered.

Bubble collisions may produce a larger signal if the bubble wall can run away. In the present model, the effective potential has a barrier at zero temperature for large h_s . Indeed, the maximum $\phi = 0$ becomes a false minimum for strong couplings. In this context, it is important to ask whether the bubble walls can run away. We have used Eqs. (66)-(68) to check for the possibility of runaway walls¹⁰. We show the result in Fig. 8 for the case $g_s = 2$. In order to obtain runaway walls, it is necessary to get very close to h_{max} (within a fraction $\Delta h/h \sim 10^{-4}$), and therefore requires a significant fine tuning (furthermore, for h_s so close to h_{max} the duration of the phase transition quickly becomes $\Delta t \gg H^{-1}$). Notice that, in Figs. 5-7, the values of h_s are not so finely tuned (cf. the values of h_s for the dots in Fig. 6 and the values reached in Fig. 8).

5.2 The MSSM

An interesting example of adding bosons in order to increase the strength of the phase transition is the Minimal Supersymmetric Standard Model (MSSM). This model has been considered for several years, either in the subject of electroweak baryogenesis (see, e.g., [62]) or in that of GW generation [18]. The MSSM contains two complex Higgs doublets

⁹For references on the sensitivity curves see section 6.

¹⁰We only considered the case $\mu = 0$, which gives more strongly first-order phase transitions.

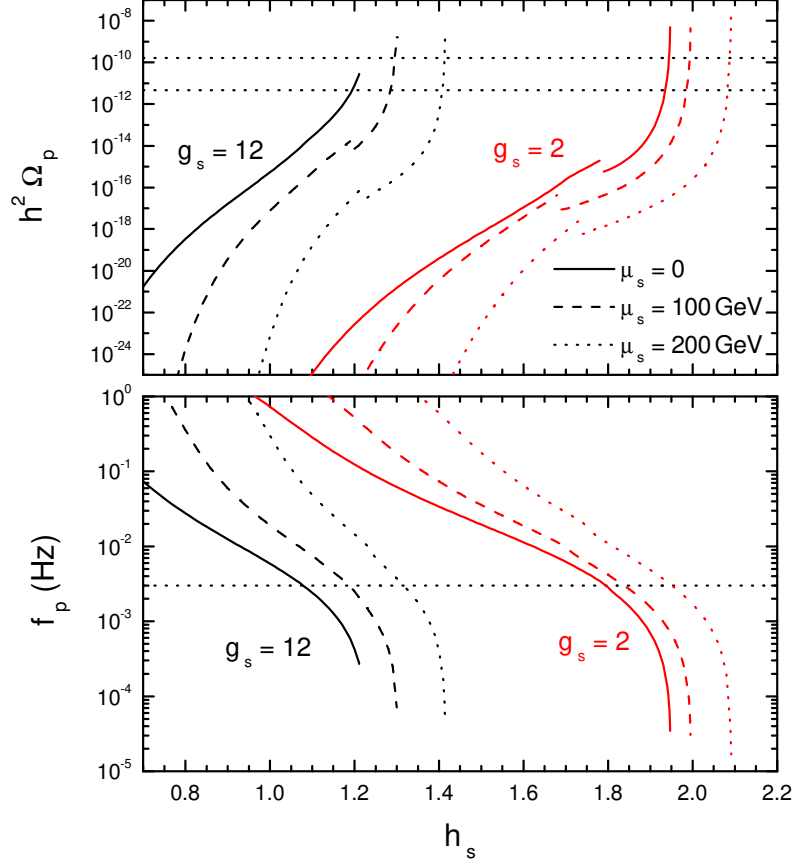


Figure 5: The energy density (top) and frequency (bottom) at the peak of the GW spectrum from turbulence, as a function of h_s for $g_s = 2$ (rightmost curves) and $g_s = 12$ (leftmost curves), with $\mu_s = 0$ (solid lines), 100 GeV (dashed lines), and 200 GeV (dotted lines). Horizontal dotted lines indicate the approximate values corresponding to the peak sensitivity of LISA and eLISA, $f \sim 1$ mHz, $h^2 \Omega_{\text{GW}} \approx 5 \times 10^{-12}$ for LISA, $h^2 \Omega_{\text{GW}} \approx 2 \times 10^{-10}$ for eLISA.

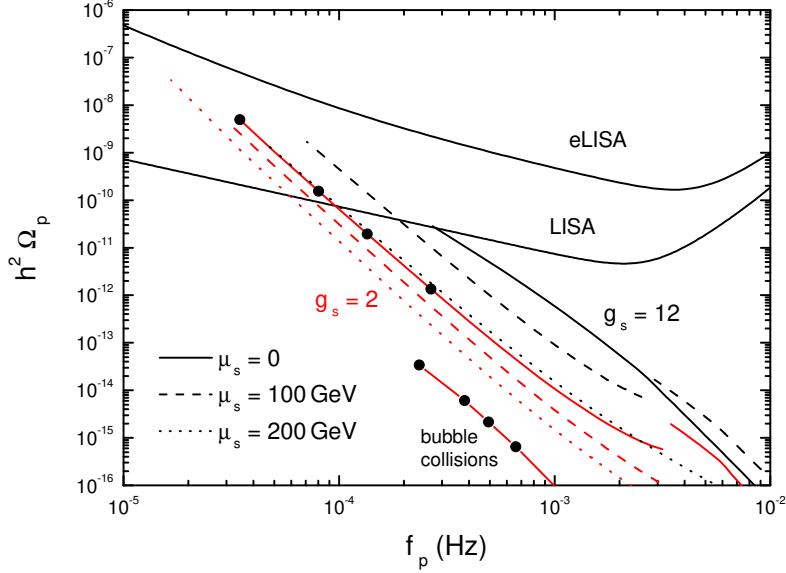


Figure 6: The peak GW signal as a function of the peak frequency for the models considered in Fig. 5, together with the sensitivity curves for LISA and eLISA. The dots on the red lines correspond (from right to left) to $h_s = 1.94, 1.943, 1.945,$ and 1.947 . The lower solid red line is the signal from bubble collisions.

H_1 and H_2 . We define the vacuum expectation values $v_1 \equiv \langle H_1^0 \rangle$ and $v_2 \equiv \langle H_2^0 \rangle$. It is customary to simplify the problem by considering the limit in which the CP-odd Higgs mass is large ($m_A \gg m_Z$). In this limit the low energy theory contains a single Higgs doublet Φ , and the masses and couplings depend on $\tan \beta \equiv v_2/v_1$. Thus, calling $\phi/\sqrt{2}$ the background of the real neutral component of Φ , the tree-level potential is of the form (56), with the quartic coupling given by $\lambda = (g^2 + g'^2) \cos^2(2\beta)/8$. Therefore, the tree-level Higgs mass is bounded by $m_H^2 < m_Z^2$. However, this tree-level relation is spoiled by radiative corrections (see e.g. [63]) and we shall consider m_H as a free parameter. The relevant SM field-dependent masses are those of the gauge bosons, $m_W^2(\phi) = g^2 \phi^2/4 \equiv h_W^2 \phi^2$, $m_Z^2(\phi) = (g^2 + g'^2) \phi^2/4 \equiv h_Z^2 \phi^2$, and top quark, $m_t^2(\phi) = h_t^2 \sin^2 \beta \phi^2/2 \equiv \bar{h}_t^2 \phi^2$, where h_t is the Yukawa coupling to H_2^0 . We shall work in the limit in which the left handed stop is heavy ($m_Q \gtrsim 500$ GeV). In this case, the one-loop correction to the SM is dominated by the right-handed top squark contribution, with a field-dependent mass given by $m_{\tilde{t}}^2(\phi) \approx m_U^2 + h_t^2 \phi^2$, where

$$h_t^2 = 0.15 h_Z^2 \cos 2\beta + \bar{h}_t^2 \left(1 - \tilde{A}_t^2/m_Q^2\right), \quad (69)$$

m_U^2 and m_Q^2 are soft breaking parameters, and \tilde{A}_t is the stop mixing parameter. If the mass of the right-handed stop is of the order of the top mass or below, the one-loop

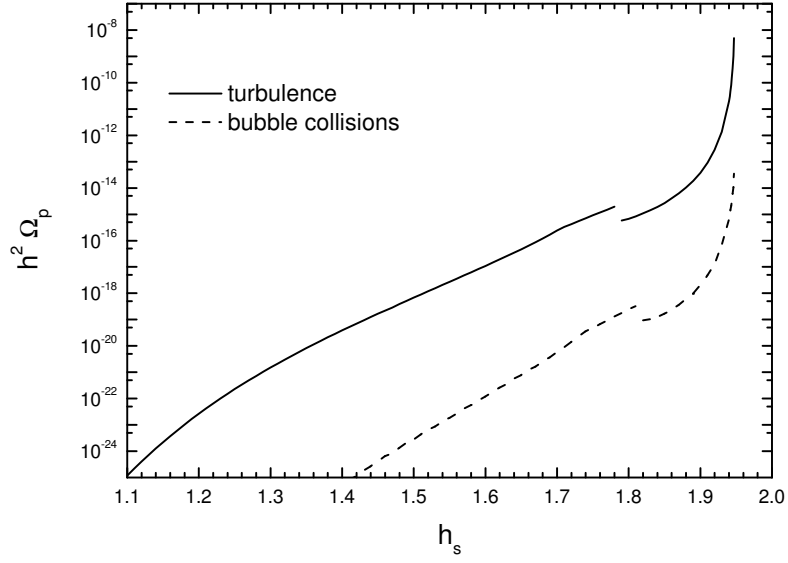


Figure 7: The peak energy density from turbulence (solid) and bubble collisions (dashed), as functions of h_s for $g_s = 2$ and $\mu_s = 0$.

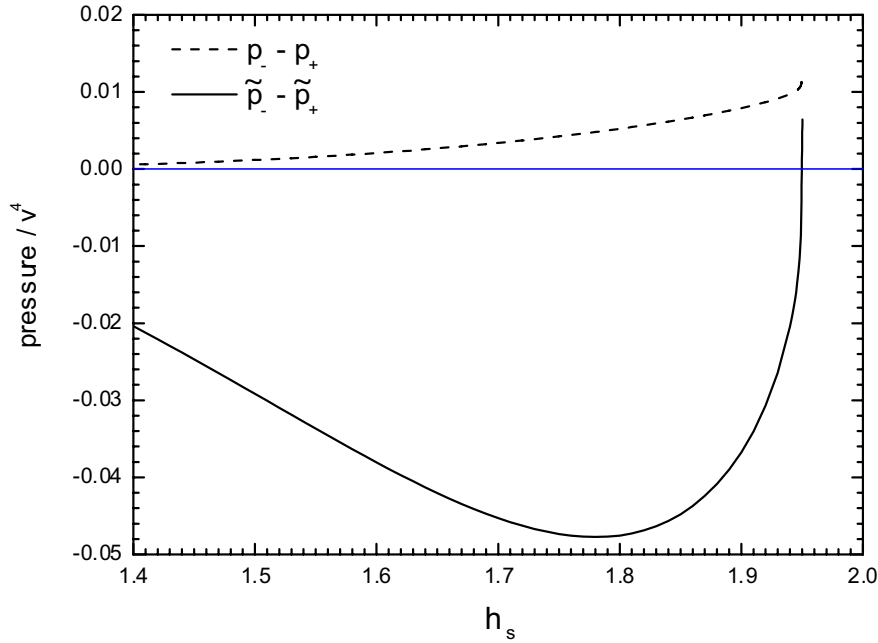


Figure 8: The pressure difference $p_- - p_+$ (dashed) and the mean field value $\tilde{p}_- - \tilde{p}_+$ (solid), as functions of h_s for $g_s = 2$ and $\mu_s = 0$. The curves are plotted up to $h_s = 1.9503$. The total force per unit area $\tilde{p}_- - \tilde{p}_+$ becomes positive at $h_s \approx 1.9497$.

effective potential admits the high-temperature expansion [62]

$$V_T(\phi) = D(T^2 - T_0^2)\phi^2 - T \left(E_{SM}\phi^3 + 6\frac{\mathcal{M}_{\tilde{t}}(\phi)^3}{12\pi} \right) + \frac{\lambda}{4}\phi^4, \quad (70)$$

where $D = m_H^2/(8v^2) + 5h_W^2/12 + 5h_Z^2/24 + h_t^2/2$ [18], $T_0^2 = m_H^2/(4D)$, E_{SM} is the cubic-term coefficient in the high-temperature expansion for the SM effective potential, $E_{SM} \approx (2h_w^3 + h_z^3)/6\pi$, and $\mathcal{M}_{\tilde{t}}^2(\phi) = m_{\tilde{t}}^2(\phi) + \Pi_{\tilde{t}}(T)$. The thermal mass is given by [62]

$$\Pi_{\tilde{t}}(T) = \left[\frac{4g_s^2}{9} + \frac{h_t^2}{6} \left(1 + \sin^2\beta \left(1 - \frac{\tilde{A}_t^2}{m_Q^2} \right) \right) + \left(\frac{1}{3} - \frac{|\cos 2\beta|}{18} \right) g'^2 \right] T^2, \quad (71)$$

where g_s is the strong gauge coupling. We shall set $\tilde{A}_t = 0$ for simplicity in the numerical calculation. The parameter T_0 gives the temperature at which the barrier between minima of the one-loop effective potential disappears. The phase transition strength is maximized for negative values of the soft mass squared $m_U^2 \approx -\Pi_{\tilde{t}}(T)$ [64], for which the contribution of the term $\mathcal{M}_{\tilde{t}}^3$ in (70) is of the form $-E_{MSSM}T\phi^3$, with a coefficient $E_{MSSM} \propto h_t^3$ that may be one order of magnitude larger than that of the SM. However, such large negative values of m_U^2 may induce the presence of color breaking minima at zero or finite temperature [65]. In order to avoid the presence of color-breaking minima, we only consider values of m_U^2 for which $m_U^2 + \Pi_{\tilde{t}}(T_0) > 0$ [18].

Nevertheless, the two-loop corrections can make the phase transition strongly first-order even for $m_U \approx 0$ [66]. The most important two-loop corrections are of the form $\phi^2 \log \phi$ and are induced by the SM weak gauge bosons, as well as by stop and gluon loops [66, 67]. In the case of a heavy left-handed stop we have [62]

$$V_2(\phi, T) \approx \frac{\phi^2 T^2}{32\pi^2} \left[\frac{51}{16} g^2 - 3 \left(2\bar{h}_t^2 \left(1 - \frac{\tilde{A}_t^2}{m_Q^2} \right) \right)^2 + 8g_s^2 2\bar{h}_t^2 \left(1 - \frac{\tilde{A}_t^2}{m_Q^2} \right) \right] \log \left(\frac{\Lambda_H}{\phi} \right), \quad (72)$$

where the scale Λ_H depends on the finite corrections and is of order 100 GeV. Following [18], we will set $\Lambda_H = 100$ GeV for the numerical computation, given the slight logarithmic dependence of V_2 on Λ_H .

In the high-temperature approximation, the friction coefficients (62) and (64) become [25, 37, 55, 56],

$$\eta_{\text{th}} = \sum \frac{g_i h_i^4}{\bar{\Gamma}/T} \left(\frac{\log \chi_i}{2\pi^2} \right)^2 \frac{\phi^2 \sigma}{T}, \quad (73)$$

$$\eta_{\text{ir}} = \sum_{\text{bosons}} \frac{g_i m_D^2 T}{32\pi L_w} \log(m_i(\phi)L_w), \quad (74)$$

where $\chi_i = 2$ for fermions and $\chi_i = m_i(\phi)/T$ for bosons, σ is the surface tension of the bubble wall, $m_D^2 \sim h_i^2 T^2$ is the Debye mass squared, and L_w is the width of the bubble wall, $L_w \approx \phi^2/\sigma$. The main contributions to the friction come from the top and the stop.

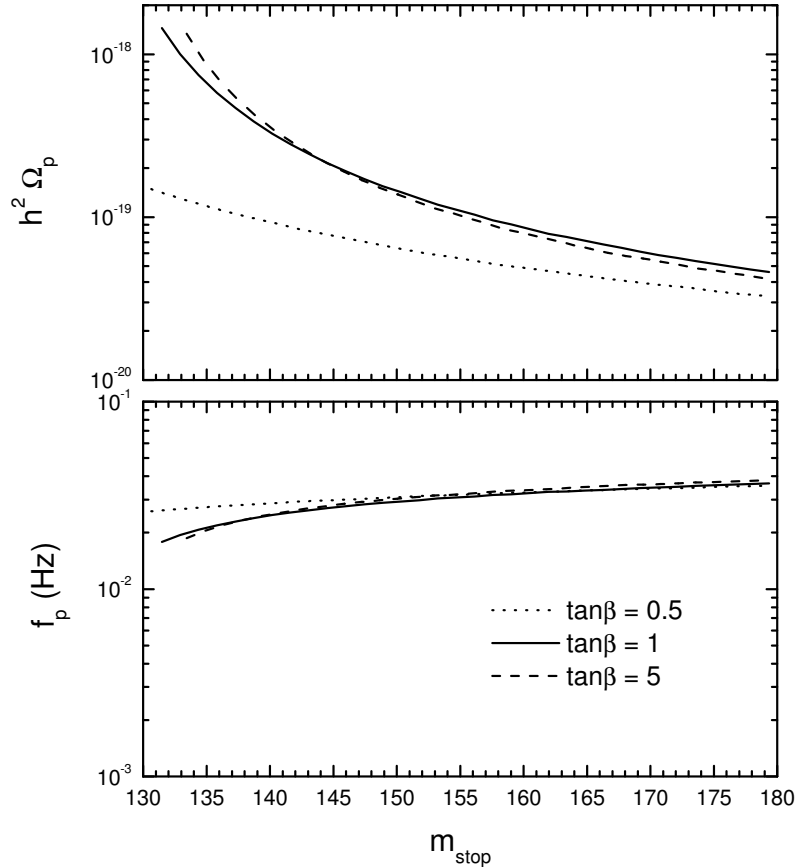


Figure 9: The peak of the GW spectrum as a function of the stop mass, for three values of $\tan\beta$.

We consider a range of values of m_U (corresponding to stop masses in the range $m_{\text{stop}} \sim 130 - 180$ GeV) which allow the high-temperature expansion (70) and avoid color-breaking minima. We find that the bubbles grow as deflagrations, with wall velocities $v_w \sim 0.4 - 0.5$ at the percolation time (slightly higher than at the onset of nucleation [37]). The shock-front velocity is $v_{\text{sh}} \approx 0.58$. In Ref. [68] a high friction (5 to 10 times larger than in an SM-like situation) was obtained using a linear extrapolation of the friction from a previous calculation. This gives wall velocities one order of magnitude smaller than ours, for which the intensity of GWs would be smaller.

Figure 9 shows the peak frequency and intensity of the GWs as a function of the stop mass for some values of $\tan\beta$. The results are quite insensitive to the value of $\tan\beta$ for $\tan\beta \sim 1$ or higher. For smaller values of $\tan\beta$, the phase transition is weaker and the intensity of GWs decreases. The results do not change significantly with m_{stop} either. The characteristic frequency is $f_p \approx 20 - 40$ mHz. The intensity of the waves is quite low, $h^2\Omega_p \lesssim 10^{-18}$, several orders of magnitude below LISA's sensitivity. This is essentially

due to the fact that the coupling of the stop to the Higgs ($h_{\bar{t}} \approx 0.7$) is relatively low (cf. Fig. 5). The use of a negative mass squared m_U^2 and the two loop correction do not make the phase transition strong enough to produce a significant GW signal.

The results should improve in the Next to Minimal Supersymmetric Standard Model (NMSSM), which consists of adding a gauge singlet to the MSSM [18, 69]. A singlet extension of the MSSM (the nearly Minimal Supersymmetric Standard Model, nMSSM) was considered in Ref. [20], finding that the GW signal is always too low to be observed by LISA or BBO. Our results for singlet extensions are more optimistic. We expect in this case a similar result to that of adding a singlet scalar to the SM, which we considered in section 5.1. The essential difference with the work [20] seems to be the fact that we considered the largest bubbles instead of those corresponding to the maximum of the volume distribution. As we have seen, this gives an enhancement factor $\log(\beta/H)$ in the bubble radius. A larger radius decreases the peak frequency as $\sim 1/R_b$ but increases the GW intensity quadratically¹¹.

Furthermore, in the NMSSM there may be cubic terms, which arise as supersymmetry-breaking soft terms. In such a case, the strength of the phase transition is dominated by the cubic terms in the tree-level potential, and it is not necessary to rely on loop corrections or to consider a light stop. As already mentioned, tree-level effects may lead to runaway walls and a larger signal from bubble collisions.

5.3 Strongly coupled extra fermions

Extra fermions strongly coupled to the Higgs field can also make the phase transition strongly first-order [70]. Strongly coupled fermions, however, make the vacuum unstable. This problem can be solved by adding heavy bosons with the same couplings but with a large ϕ -independent mass term, so that they are decoupled from the dynamics at $T \sim 100$ GeV. The model can be considered as a particular realization of split supersymmetry, where the standard relations between the Yukawa and gauge couplings are not fulfilled. In the simplest case, only $g_f = 12$ d.o.f. are coupled to the SM Higgs, with degenerate eigenvalues of the form $m_f^2(\phi) = \mu_f^2 + h_f^2 \phi^2$. Perturbativity requires $h_f \lesssim 3.5$. The bosonic stabilizing fields have the same number of d.o.f., and a dispersion relation $m_s^2(\phi) = \mu_s^2 + h_s^2 \phi^2$, with $h_s = h_f$. For simplicity, $\Pi_s = 0$ is assumed. Following [70], we shall set μ_s to the maximum value consistent with stability,

$$\mu_s^2 = \exp\left(\frac{m_H^2 8\pi^2}{g_f h_f^4 v^2}\right) m_f^2(v) - h_f^2 v^2. \quad (75)$$

In Fig. 10 we have plotted the peak frequency and peak intensity of GWs as a function of h_f , for several values of μ_f . Notice that, for high values of the Yukawa coupling h_f , this model gives mHz frequencies and a GW signal $h^2 \Omega_p \sim 10^{-15}$, stronger than the MSSM. However, the signal is still below LISA's sensitivity. The problem with the extra fermions is that, compared to the case of bosons, larger values of the coupling h_f are needed to

¹¹Notice also that reaching LISA's sensitivity in section 5.1 required a certain fine tuning of the parameters. The analysis of Ref. [20] uses randomly chosen values of the parameters, which may not enter the fine tuning region.

obtain a strongly first-order phase transition. Larger values of h_f cause a larger friction coefficient. As a consequence, the wall velocity is smaller than in models with extra bosons (for a phase transition of the same strength). We find velocities $v_w \lesssim 0.2$, and as small as $v_w = 0.05$ for strongly first-order phase transitions. This makes this model interesting for baryogenesis, since the generated baryon asymmetry peaks for $v_w \ll 1$ [71], but not for GW generation.

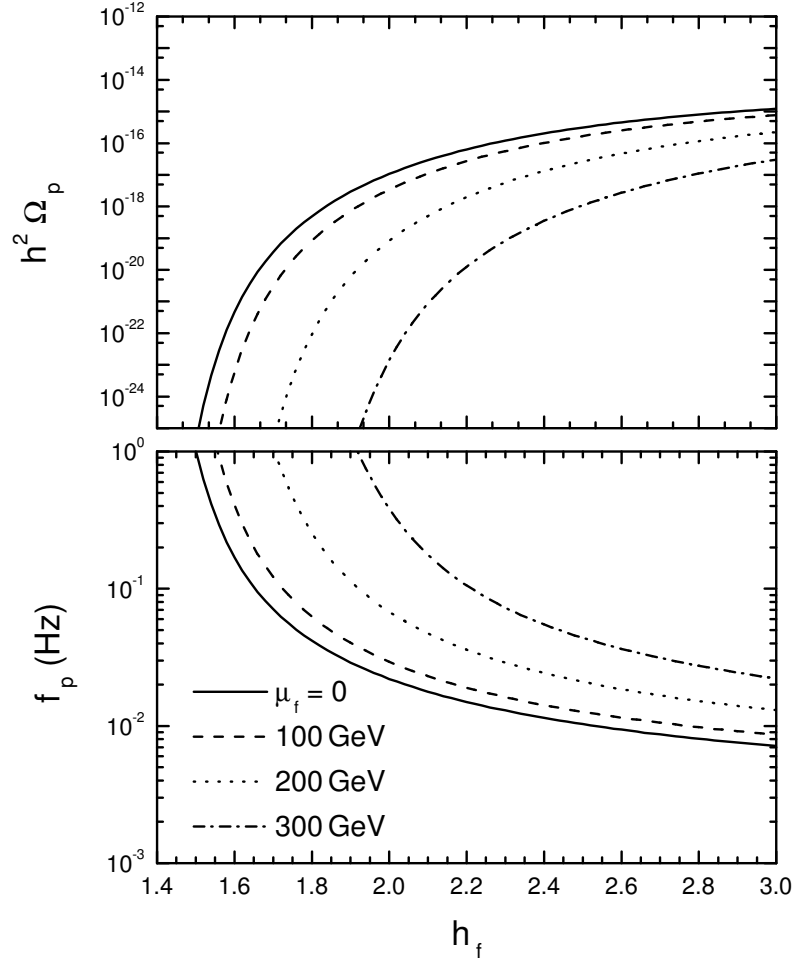


Figure 10: The peak of the GW spectrum as a function of h_f for several values of μ_f .

6 Detectability of electroweak gravitational waves: LISA and beyond

In this section we shall compare the results for the models we have considered for the electroweak phase transition, and we shall discuss the detectability of the predicted grav-

itational waves. We show in Fig. 11 some representative curves from each of the models, together with the projected sensitivities of several detectors. For comparison, we also show other sources of a stochastic GW background, such as galactic and extragalactic binaries [72] and inflation. The CMB and large-scale structure constrain the scale of inflation to be below 3.4×10^{16} GeV, fixing the largest signal expected from inflation [10] to $h^2\Omega_{\text{GW}} \sim 10^{-14}$. Interestingly, for the models we considered, GW signals which are high enough to be detected by LISA, are separated in frequency from the noise of white dwarf binaries.

In general, a GW signal of electroweak scale origin lies far away from the sensitivities of ground-based detectors such as LIGO or its successors Advanced LIGO, LIGO III, which peak at $f \sim 100$ Hz. Therefore, we shall consider spaceborne detectors. The sensitivity curves in Fig. 11 are approximate. The sensitivity for eLISA (upper blue line) was calculated using the analytical approximation from Ref. [3]. The other sensitivities were calculated from the specifications of the detectors, following the method described in Ref. [73]. Specifications for LISA (lower blue line) can be found in [2, 73], specifications for BBO (upper purple curve) can be found in [4] and specifications for DECIGO (upper orange curve) can be found in [5, 6]. Being composed of several LISA type detectors, the latter two will be able to make a correlation analysis between two independent detectors. The correlation analysis is expected to increase the sensitivity of BBO to a stochastic background by four orders of magnitude [10, 32, 74] (lower purple curve). On the other hand, the ultimate sensitivity of DECIGO is estimated to be $h^2\Omega_{\text{GW}} \sim 10^{-20}$ around 0.1 Hz [5, 10] (lower orange curve).

The predicted signals for the different models are shown in black in Fig. 11. For all the models we considered, the parameters which give frequencies at the sensitivity peak of LISA ($f \sim 1$ mHz) give intensities a few orders of magnitude below the peak sensitivity $h^2\Omega_{\text{GW}} \sim 10^{-12}$. We see that LISA's sensitivity curve is instead achieved at characteristic frequencies $f_p \sim 10^{-4}$ Hz, by somewhat extreme models, namely, those with extra scalars with quite strong couplings to the Higgs. Subsequent detectors like BBO or the Japanese DECIGO will have a sensitivity peak about two orders of magnitude below that of LISA, $h^2\Omega_{\text{GW}} \sim 10^{-14}$ - 10^{-13} . However, this peak sensitivity will be for a frequency $f \sim 0.1$ Hz – 1 Hz, far away from electroweak GW signals of that intensity. As can be seen in the figure, neither BBO nor DECIGO will, in principle, improve LISA's possibility of detecting a GW signal from the electroweak phase transition. Nevertheless, after a correlation analysis, BBO will possibly be able to detect electroweak GWs for a wider range of SM extensions, e.g., extra bosons with moderate couplings or strongly coupled extra fermions. The detection would be further improved by the ultimate sensitivity of DECIGO. The latter seems to be the only possibility for detecting electroweak gravitational waves in the case of the MSSM. In the case of the NMSSM we expect a signal similar to that of the SM with an extra singlet.

7 Conclusions

We have calculated the intensity and characteristic frequency of gravitational radiation generated in the electroweak phase transition. We have considered several extensions of

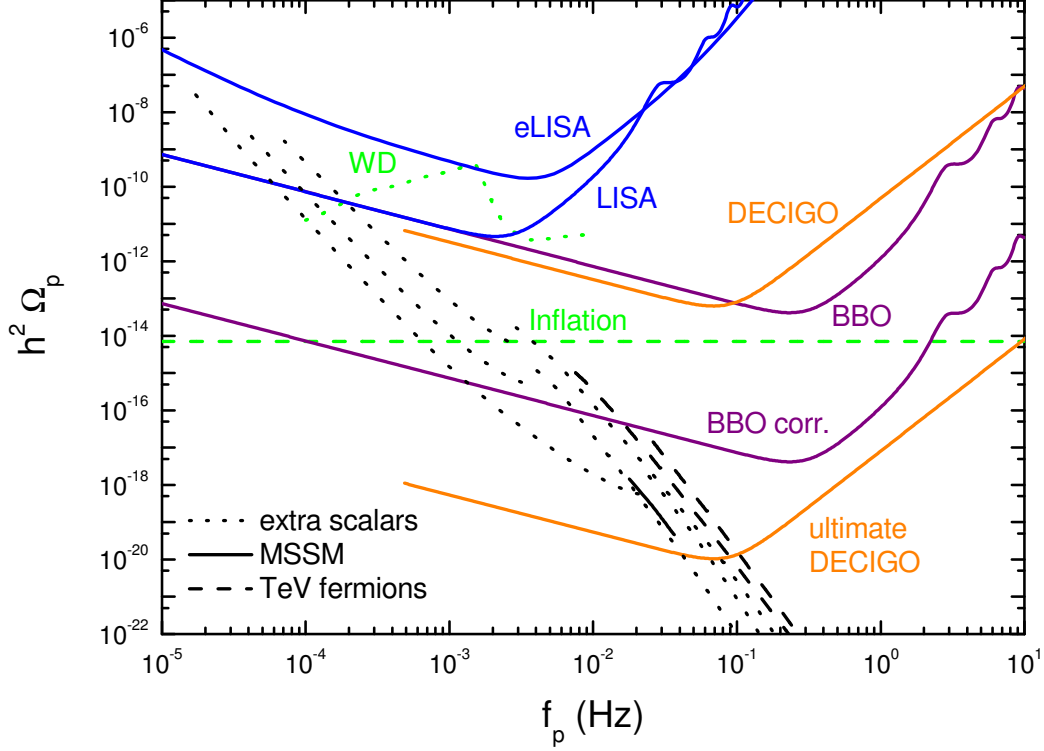


Figure 11: The predicted value of Ω_{GW} at the peak of the spectrum as a function of the peak frequency, for different models, together with the noise from other stochastic sources, and the sensitivities of several spaceborne laser interferometer gravitational wave observatories. The upper blue line is the sensitivity curve for eLISA, the lower blue line is the one for LISA, the upper purple line is for BBO, the lower purple line for BBO correlated, the upper orange line for DECIGO, and the lower orange curve for the ultimate sensitivity of DECIGO. The dotted green line corresponds to the signal from white dwarf binaries (WD), and the dashed green line is the maximum signal expected from inflation. Dotted black curves correspond to SM extensions with extra scalars. From left to right, we have $g_s = 2$ d.o.f. with invariant mass $\mu_s = 200$ GeV and $\mu_s = 0$, and $g_s = 12$ with $\mu_s = 100$ GeV. The intensity of GWs increases with the coupling h_s to the Higgs. The solid black curve corresponds to the MSSM for $\tan\beta = 1$. The intensity of GWs is higher for lower values of the stop mass. Dashed black lines correspond to extensions with strongly coupled fermions with $g_f = 12$ and $\mu_f = 0$ (leftmost curve) and $\mu_f = 300$ GeV (rightmost curve). In these curves, the GW signal increases with h_f .

the Standard Model which provide strongly first-order phase transitions, and we have discussed the detectability of these models by planned spaceborne gravitational wave detectors.

We have improved the treatment of previous works on the dynamics of the phase transition by including in the calculation the hydrodynamics and microphysics of the bubble walls. Most works on GWs assume that the bubble walls propagate as Jouguet detonations. In contrast, we have determined, as a function of the temperature, whether the walls propagate as subsonic or supersonic deflagrations, or as weak detonations. We have also taken into account the possibility that, instead of reaching a stationary state, the walls run away. In order to determine the hydrodynamic solution we have estimated the friction for each model, using approximations derived in Refs. [25, 37]. These approximations do not depend on details of the specific model and have the correct dependence on the relevant parameters (e.g. the couplings of the extra particles with the Higgs). Thus, our wall velocity depends on the friction coefficient as well as on the thermodynamic parameters.

Furthermore, we have numerically evolved the phase transition from the nucleation of the first bubbles until the time of bubble percolation, taking into account the variation of the nucleation rate and of the wall velocity with temperature. We have also taken into account the fact that the nucleation rate is suppressed in the regions that are reheated by shock fronts. We accomplished this in a simple way by considering the fraction of volume occupied by “shock front bubbles”.

The evolution of the phase transition was considered in some detail in Refs. [20] and [22]. The latter studied an extension of the SM with extra scalars. However, only bubble collisions were considered as a source of GWs. As we have seen, the signal from bubble collisions is generally much lower than that from turbulence (at least for phase transitions which do not have runaway bubble walls). The work of Ref. [20], on the other hand, considered both signals from bubble collisions and turbulence, and models which, in principle, may give stronger phase transitions. However, the relevant size scale of the turbulence was assumed to correspond to the bubbles which maximize the volume distribution at the percolation time. In contrast, we have argued that the relevant wavelength is given by the size of the largest bubbles. We obtain a higher signal, since the intensity of the GWs is higher for larger bubbles ($\rho_{\text{GW}} \sim R_b^2$). As we have seen, the size of the largest bubbles can be approximated by $R_b \approx 3v_w\beta^{-1}\log(\beta/H)$, and there is an enhancement $\log(\beta/H)$ with respect to the size corresponding to maximum volume. It is clear that further investigation is needed in order to determine the spectrum of turbulence in the presence of several stirring scales (in the case of a phase transition, a continuum of bubble sizes).

For most of the models and parameters, the gravitational wave signal from the electroweak phase transition seems to be rather weak to be detected by LISA. Nevertheless, extensions with scalar singlets which are strongly coupled to the Higgs give considerably strong phase transitions, which produce GWs with intensities as high as $h^2\Omega_{\text{GW}} \sim 10^{-8}$ for frequencies $f \lesssim 10^{-4}$ Hz. These models give a signal detectable by LISA, although some fine tuning of the parameters (below the 1% level) is required. Taking into account that the sensitivity curves are only approximate, and that current calculations of GW generation and phase transition dynamics may have large errors, this fine tuning may

be relaxed in the future. The extension of the SM with strongly coupled fermions gives weaker signals, which could be detected after a correlation analysis from BBO. For the case of the MSSM, the ultimate sensitivity of DECIGO would be needed to detect GWs from the electroweak phase transition.

Interestingly, the model with extra fermions gives a larger signal than the MSSM, even though the wall velocity is smaller. This confirms the importance of taking into account the complete dynamics of the phase transition. To begin with, the wall velocity is not directly related to the strength of the phase transition. For instance, two models may have the same amount of supercooling and quite different friction, thus giving different wall velocities. Most importantly, the GW intensity further depends on the size of the largest bubbles, which is rather unpredictable without a careful analysis, due to the nontrivial dynamics of nucleation and reheating. Thus, higher wall velocities do not always guarantee larger bubble radii.

Acknowledgements

This work was supported in part by Universidad Nacional de Mar del Plata, Argentina, grants EXA 473/10 and 505/10. The work by A.D.S. was supported by CONICET through project PIP 122-201009-00315. The work by A.M. and L.L. was supported by CONICET through project PIP 112-200801-00943. L.L. is supported by fellowship from CIC (Buenos Aires, Argentina).

References

- [1] M. Maggiore, Phys. Rept. **331**, 283 (2000) [gr-qc/9909001].
- [2] K. Danzmann and A. Rudiger, Class. Quant. Grav. **20**, S1 (2003).
- [3] P. Amaro-Seoane, S. Aoudia, S. Babak, P. Binetruy, E. Berti, A. Bohe, C. Caprini and M. Colpi *et al.*, arXiv:1201.3621 [astro-ph.CO].
- [4] V. Corbin and N. J. Cornish, Class. Quant. Grav. **23** (2006) 2435 [gr-qc/0512039]; C. Ungarelli, P. Corasaniti, R. A. Mercer and A. Vecchio, Class. Quant. Grav. **22**, S955 (2005) [astro-ph/0504294]; C. Cutler and J. Harms, Phys. Rev. D **73**, 042001 (2006) [gr-qc/0511092]; G. M. Harry, P. Fritschel, D. A. Shaddock, W. Folkner and E. S. Phinney, Class. Quant. Grav. **23**, 4887 (2006) [Erratum-ibid. **23**, 7361 (2006)].
- [5] N. Seto, S. Kawamura and T. Nakamura, Phys. Rev. Lett. **87**, 221103 (2001) [astro-ph/0108011].
- [6] S. Kawamura, T. Nakamura, M. Ando, N. Seto, K. Tsubono, K. Numata, R. Takahashi and S. Nagano *et al.*, Class. Quant. Grav. **23**, S125 (2006); S. Kawamura *et al.*, J. Phys.: Conf. Ser. 122, 012006 (2008).
- [7] M. Maggiore, “Gravitational Waves. Vol. 1: Theory and Experiments,” Oxford University Press, October 2007. 572p. (ISBN-13: 978-0-19-857074-5).

- [8] S. Babak, J. R. Gair, A. Petiteau and A. Sesana, *Class. Quant. Grav.* **28**, 114001 (2011) [arXiv:1011.2062 [gr-qc]].
- [9] P. Binetruy, A. Bohe, C. Caprini and J. -F. Dufaux, arXiv:1201.0983 [gr-qc].
- [10] T. L. Smith, M. Kamionkowski and A. Cooray, *Phys. Rev. D* **73**, 023504 (2006) [astro-ph/0506422].
- [11] A. Kusenko and A. Mazumdar, *Phys. Rev. Lett.* **101**, 211301 (2008) [arXiv:0807.4554 [astro-ph]]; A. Kusenko, A. Mazumdar and T. Multamaki, *Phys. Rev. D* **79**, 124034 (2009) [arXiv:0902.2197 [astro-ph.CO]].
- [12] A. Vilenkin, *Phys. Rept.* **121**, 263 (1985); B. Allen, In *Les Houches 1995, Relativistic gravitation and gravitational radiation* 373-417 [gr-qc/9604033].
- [13] C. Caprini and R. Durrer, *Phys. Rev. D* **74**, 063521 (2006) [astro-ph/0603476].
- [14] A. Kosowsky, A. Mack and T. Kahniashvili, *Phys. Rev. D* **66**, 024030 (2002) [astro-ph/0111483].
- [15] M. S. Turner and F. Wilczek, *Phys. Rev. Lett.* **65**, 3080 (1990); *Phys. Rev. Lett.* **69**, 2026 (1992); A. Kosowsky and M. S. Turner, *Phys. Rev. D* **47**, 4372 (1993).
- [16] A. Kosowsky, M. S. Turner and R. Watkins, *Phys. Rev. D* **45**, 4514 (1992).
- [17] M. Kamionkowski, A. Kosowsky and M. S. Turner, *Phys. Rev. D* **49**, 2837 (1994).
- [18] R. Apreda, M. Maggiore, A. Nicolis and A. Riotto, *Nucl. Phys. B* **631**, 342 (2002).
- [19] A. Nicolis, *Class. Quant. Grav.* **21**, L27 (2004); C. Grojean and G. Servant, *Phys. Rev. D* **75**, 043507 (2007); T. Kahniashvili, A. Kosowsky, G. Gogoberidze and Y. Maravin, *Phys. Rev. D* **78**, 043003 (2008) [arXiv:0806.0293 [astro-ph]].
- [20] S. J. Huber and T. Konstandin, *JCAP* **0805**, 017 (2008) [arXiv:0709.2091 [hep-ph]].
- [21] A. Mégevand, *Phys. Rev. D* **78** (2008) 084003 [arXiv:0804.0391 [astro-ph]].
- [22] J. R. Espinosa, T. Konstandin, J. M. No and M. Quiros, *Phys. Rev. D* **78**, 123528 (2008) [arXiv:0809.3215 [hep-ph]].
- [23] J. Kehayias and S. Profumo, *JCAP* **1003**, 003 (2010) [arXiv:0911.0687 [hep-ph]].
- [24] A. Mégevand, *Int. J. Mod. Phys. D* **9**, 733 (2000) [hep-ph/0006177].
- [25] A. Mégevand, *Phys. Rev. D* **69**, 103521 (2004).
- [26] A. Mégevand and A. D. Sánchez, *Phys. Rev. D* **77**, 063519 (2008) [arXiv:0712.1031 [hep-ph]].
- [27] S. J. Huber and T. Konstandin, *JCAP* **0809**, 022 (2008) [arXiv:0806.1828 [hep-ph]].

- [28] C. Caprini, R. Durrer and G. Servant, Phys. Rev. D **77**, 124015 (2008) [arXiv:0711.2593 [astro-ph]].
- [29] A. D. Dolgov, D. Grasso and A. Nicolis, Phys. Rev. D **66**, 103505 (2002).
- [30] G. Gogoberidze, T. Kahniashvili and A. Kosowsky, Phys. Rev. D **76**, 083002 (2007).
- [31] T. Kahniashvili, G. Gogoberidze and B. Ratra, arXiv:0802.3524 [astro-ph].
- [32] C. Caprini, R. Durrer and G. Servant, JCAP **0912**, 024 (2009) [arXiv:0909.0622 [astro-ph.CO]].
- [33] W. Buchmuller and O. Philipsen, Nucl. Phys. B **443**, 47 (1995) [hep-ph/9411334]; K. Kajantie, M. Laine, K. Rummukainen and M. E. Shaposhnikov, Phys. Rev. Lett. **77**, 2887 (1996) [hep-ph/9605288].
- [34] For reviews, see A. G. Cohen, D. B. Kaplan and A. E. Nelson, Ann. Rev. Nucl. Part. Sci. **43**, 27 (1993) [arXiv:hep-ph/9302210]; A. Riotto and M. Trodden, Ann. Rev. Nucl. Part. Sci. **49**, 35 (1999) [arXiv:hep-ph/9901362].
- [35] M. Gyulassy, K. Kajantie, H. Kurki-Suonio and L. D. McLerran, Nucl. Phys. B **237**, 477 (1984); H. Kurki-Suonio, Nucl. Phys. B **255**, 231 (1985); K. Kajantie and H. Kurki-Suonio, Phys. Rev. D **34**, 1719 (1986); K. Enqvist, J. Ignatius, K. Kajantie and K. Rummukainen, Phys. Rev. D **45**, 3415 (1992); A. F. Heckler, Phys. Rev. D **51** 405, (1995) [arXiv:astro-ph/9407064].
- [36] A. Mégevand and A. D. Sánchez, Nucl. Phys. B **820**, 47 (2009) [arXiv:0904.1753 [hep-ph]].
- [37] A. Mégevand and A. D. Sánchez, Nucl. Phys. B **825**, 151 (2010) [arXiv:0908.3663 [hep-ph]].
- [38] J. R. Espinosa, T. Konstandin, J. M. No and G. Servant, JCAP **1006**, 028 (2010) [arXiv:1004.4187 [hep-ph]]; T. Konstandin and J. M. No, JCAP **1102**, 008 (2011) [arXiv:1011.3735 [hep-ph]].
- [39] D. Bodeker and G. D. Moore, JCAP **0905**, 009 (2009) [arXiv:0903.4099 [hep-ph]].
- [40] L. Leitao and A. Mégevand, Nucl. Phys. B **844**, 450 (2011) [arXiv:1010.2134 [astro-ph.CO]].
- [41] T. Kahniashvili, L. Campanelli, G. Gogoberidze, Y. Maravin and B. Ratra, Phys. Rev. D **78**, 123006 (2008) [Erratum-ibid. D **79**, 109901 (2009)] [arXiv:0809.1899 [astro-ph]]; T. Kahniashvili, L. Kisslinger and T. Stevens, arXiv:0905.0643 [astro-ph.CO].
- [42] A. Mégevand and A. D. Sánchez, Nucl. Phys. B **865**, 217 (2012) [arXiv:1206.2339 [astro-ph.CO]].

- [43] K. Nakamura et al. (Particle Data Group), J. Phys. G **37**, 075021 (2010) and 2011 partial update for the 2012 edition.
- [44] C. Caprini, R. Durrer and X. Siemens, Phys. Rev. D **82**, 063511 (2010) [arXiv:1007.1218 [astro-ph.CO]].
- [45] L. D. Landau and E. M. Lifshitz, *Fluid Mechanics* (Pergamon Press, New York, 1989); R. Courant and K. O. Friedrichs, *Supersonic Flow and Shock Waves* (Springer-Verlag, Berlin, 1985).
- [46] P. J. Steinhardt, Phys. Rev. D **25**, 2074 (1982).
- [47] J. Ignatius, K. Kajantie, H. Kurki-Suonio and M. Laine, Phys. Rev. D **49**, 3854 (1994); H. Kurki-Suonio and M. Laine, Phys. Rev. D **51**, 5431 (1995) [arXiv:hep-ph/9501216]; H. Kurki-Suonio and M. Laine, Phys. Rev. D **54**, 7163 (1996) [hep-ph/9512202].
- [48] V.K.S. Shante and S. Kirkpatrick, Adv. Phys. **20**, 325 (1971). See also T. Çelik, F. Karsch and H. Satz, Phys. Lett. B **97**, 128 (1980).
- [49] S. R. Coleman, Phys. Rev. D **15**, 2929 (1977) [Erratum-ibid. D **16**, 1248 (1977)]; C. G. Callan and S. R. Coleman, Phys. Rev. D **16**, 1762 (1977).
- [50] I. Affleck, Phys. Rev. Lett. **46**, 388 (1981); A. D. Linde, Nucl. Phys. B **216**, 421 (1983) [Erratum-ibid. B **223**, 544 (1983)]; Phys. Lett. B **100**, 37 (1981).
- [51] A. H. Guth and E. J. Weinberg, Phys. Rev. D **23**, 876 (1981).
- [52] G. W. Anderson and L. J. Hall, Phys. Rev. D **45**, 2685 (1992).
- [53] M. Quiros, arXiv:hep-ph/9901312.
- [54] C. Wainwright, S. Profumo and M. J. Ramsey-Musolf, Phys. Rev. D **84**, 023521 (2011) [arXiv:1104.5487 [hep-ph]]; C. L. Wainwright, S. Profumo and M. J. Ramsey-Musolf, arXiv:1204.5464 [hep-ph].
- [55] B. H. Liu, L. D. McLerran and N. Turok, Phys. Rev. D **46**, 2668 (1992); N. Turok, Phys. Rev. Lett. **68**, 1803 (1992); M. Dine, R. G. Leigh, P. Y. Huet, A. D. Linde and D. A. Linde, Phys. Rev. D **46**, 550 (1992) [arXiv:hep-ph/9203203]; S. Y. Khlebnikov, Phys. Rev. D **46**, 3223 (1992); P. Arnold, Phys. Rev. D **48**, 1539 (1993) [arXiv:hep-ph/9302258]; G. D. Moore and T. Prokopec, Phys. Rev. D **52**, 7182 (1995) [arXiv:hep-ph/9506475]; Phys. Rev. Lett. **75**, 777 (1995) [arXiv:hep-ph/9503296]; P. John and M. G. Schmidt, Nucl. Phys. B **598**, 291 (2001) [Erratum-ibid. B **648**, 449 (2003)].
- [56] G. D. Moore, JHEP **0003**, 006 (2000); G. D. Moore and N. Turok, Phys. Rev. D **55**, 6538 (1997) [arXiv:hep-ph/9608350].
- [57] M. Dine, P. Huet, R. L. Singleton and L. Susskind, Phys. Lett. B **257**, 351 (1991); M. Dine, P. Huet and R. L. . Singleton, Nucl. Phys. B **375**, 625 (1992).

- [58] J. Choi and R. R. Volkas, Phys. Lett. B **317**, 385 (1993) [arXiv:hep-ph/9308234]; S. W. Ham, Y. S. Jeong and S. K. Oh, J. Phys. G **31**, 857 (2005) [arXiv:hep-ph/0411352].
- [59] J. R. Espinosa and M. Quiros, Phys. Lett. B **305**, 98 (1993) [arXiv:hep-ph/9301285].
- [60] A. Ahriche, Phys. Rev. D **75**, 083522 (2007) [arXiv:hep-ph/0701192]; S. Profumo, M. J. Ramsey-Musolf and G. Shaughnessy, JHEP **0708**, 010 (2007) [arXiv:0705.2425 [hep-ph]]; A. Ashoorioon and T. Konstandin, arXiv:0904.0353 [hep-ph].
- [61] J. R. Espinosa and M. Quiros, Phys. Rev. D **76**, 076004 (2007) [arXiv:hep-ph/0701145].
- [62] M. S. Carena, M. Quiros and C. E. M. Wagner, Nucl. Phys. B **524**, 3 (1998) [arXiv:hep-ph/9710401].
- [63] J. A. Casas, J. R. Espinosa, M. Quiros and A. Riotto, Nucl. Phys. B **436**, 3 (1995) [Erratum-ibid. B **439**, 466 (1995)] [arXiv:hep-ph/9407389].
- [64] M. S. Carena, M. Quiros and C. E. M. Wagner, Phys. Lett. B **380**, 81 (1996) [arXiv:hep-ph/9603420].
- [65] M. S. Carena and C. E. M. Wagner, Nucl. Phys. B **452**, 45 (1995) [arXiv:hep-ph/9408253].
- [66] J. R. Espinosa, Nucl. Phys. B **475**, 273 (1996) [arXiv:hep-ph/9604320].
- [67] J. E. Bagnasco and M. Dine, Phys. Lett. B **303**, 308 (1993) [arXiv:hep-ph/9212288]; P. Arnold and O. Espinosa, Phys. Rev. D **47**, 3546 (1993) [Erratum-ibid. D **50**, 6662 (1994)] [arXiv:hep-ph/9212235]; Z. Fodor and A. Hebecker, Nucl. Phys. B **432**, 127 (1994) [arXiv:hep-ph/9403219].
- [68] S. J. Huber and M. Sopena, Phys. Rev. D **85**, 103507 (2012) [arXiv:1112.1888 [hep-ph]].
- [69] M. Pietroni, Nucl. Phys. B **402**, 27 (1993) [arXiv:hep-ph/9207227]; A. T. Davies, C. D. Froggatt and R. G. Moorhouse, Phys. Lett. B **372**, 88 (1996) [arXiv:hep-ph/9603388]; S. J. Huber and M. G. Schmidt, Nucl. Phys. B **606**, 183 (2001) [arXiv:hep-ph/0003122].
- [70] M. S. Carena, A. Megevand, M. Quiros and C. E. M. Wagner, Nucl. Phys. B **716**, 319 (2005) [arXiv:hep-ph/0410352].
- [71] A. E. Nelson, D. B. Kaplan and A. G. Cohen, Nucl. Phys. B **373**, 453 (1992); J. M. Cline and K. Kainulainen, Phys. Rev. Lett. **85**, 5519 (2000) [arXiv:hep-ph/0002272]; J. M. Cline, M. Joyce and K. Kainulainen, JHEP **0007**, 018 (2000) [arXiv:hep-ph/0006119]; M. Carena, J. M. Moreno, M. Quiros, M. Seco and C. E. Wagner, Nucl. Phys. B **599**, 158 (2001) [arXiv:hep-ph/0011055].

- [72] P. L. Bender and D. Hils, *Class. Quant. Grav.* **14**, 1439 (1997); W. A. Hiscock, S. L. Larson, J. R. Routzahn and B. Kulick, *Astrophys. J.* **540**, L5 (2000) [gr-qc/0005134]. Data for the WD curve can be obtained in <http://www.srl.caltech.edu/~shane/sensitivity/MakeCurve.html>.
- [73] S. L. Larson, W. A. Hiscock and R. W. Hellings, *Phys. Rev. D* **62**, 062001 (2000) [gr-qc/9909080]. We used the sensitivity curve generator in Shane Larson's web page <http://www.srl.caltech.edu/shane/sensitivity/MakeCurve.html>, where the specifications for LISA can be found.
- [74] A. Buonanno, G. Sigl, G. G. Raffelt, H. -T. Janka and E. Muller, *Phys. Rev. D* **72**, 084001 (2005) [astro-ph/0412277]; A. Cooray, *Mod. Phys. Lett. A* **20**, 2503 (2005) [astro-ph/0503118]; M. Maggiore, gr-qc/0008027.